Magneto-optical spectra of the split nickel-vacancy defect in diamond

Gergő Thiering* and Adam Gali†
Wigner Research Centre for Physics, P.O. Box 49, H-1525, Budapest, Hungary
and Department of Atomic Physics, Budapest University of Technology and Economics, Budafoki út 8., H-1111 Budapest, Hungary

(Received 28 July 2021; accepted 29 September 2021; published 19 October 2021)

Nickel is a common impurity in high-pressure high-temperature diamond and may contaminate chemical vapor deposited diamond used for high-power electronics or quantum technology applications. Magneto-optical fingerprints of nickel have been known since decades, however, no consensus has been reached about the microscopic origins of nickel-related electron paramagnetic resonance, photoluminescence, and optically detected magnetic resonance spectra. The unknown nickel-related defect structures in diamond make it difficult to control them or harness them for a given application. As a consequence, nickel is considered as an impurity in diamond that should be avoided or its concentration should be minimized. Recent advances in the development of *ab initio* magneto-optical spectroscopy have significantly increased its accuracy and predictive power that can be employed for identification and in-depth characterization of paramagnetic color centers in diamond. In this study, we extend the accuracy of the *ab initio* magneto-optical spectroscopy tools towards self-consistent calculation of second-order spin-orbit coupling for paramagnetic color centers in solids. We apply the full arsenal of the *ab initio* magneto-optical spectroscopy tools to characterize the split nickel-vacancy defect in diamond which is one of the most stable nickel-related defect configurations. As a result, electron paramagnetic resonance and optical centers are positively identified in various charge states of the nickel-vacancy defect in diamond. In particular, the 1.40-eV optical center and the NIRIM-2 electron paramagnetic resonance center are identified as the single negative charge state of the split nickel-vacancy center. The defect possesses $S = \frac{1}{2}$ spin state with an orbital doublet ground state. We find that the coherence time of the ground-state spin is about 0.1 ms at cryogenic temperatures which can be optically initialized and readout by a Λ-scheme protocol. Since the defect has inversion symmetry the optical signal is insensitive to the stray electric fields, which is an advantage for creating indistinguishable solid-state single-photon sources. We predict that the negatively charged nickel-vacancy defect has similar optical properties to those of the well-known silicon-vacancy defect in diamond but is superior in terms of electron spin coherence times. Our study resolves a few decades controversy about the nickel-related spectroscopy centers in diamond and turns nickel from an impurity to a resource in quantum technology applications.

DOI: 10.1103/PhysRevResearch.3.043052

I. INTRODUCTION

Nickel is a typical contaminant in high-pressure high-temperature (HPHT) diamonds that produced fingerprints in various nickel-related optical and electron paramagnetic resonance (EPR) centers in diamond [1–3]. However, most of the assignments of the optical and EPR centers to defect structures were only tentative. The advance in the accurate characterization of defects in solids by means of first-principles calculations makes possible to identify the origin of these centers by comparing the experimental and *ab initio* magneto-optical spectra as demonstrated for color centers in diamond [4–6]. It has been recently found in a joint experimental and theoretical study [7] that the split nickel-vacancy complex produces photocurrent signals which could be a potential readout technique for the electron [8–11] and nuclear spins [12,13] of nickel defects in diamond. In this paper, we determine the magneto-optical properties of the split nickel-vacancy complex by means of *ab initio* calculations and associate those to the already reported nickel-related optical and EPR signals. By identification of the nickel-related paramagnetic color centers, one can identify the target defect spins for quantum technology applications and can mediate understanding the role of nickel in the HPHT diamond synthesis process.

The first EPR center that was associated with nickel (Ni) in diamond was the W8 center reported in 1966 [14]. The presence of Ni in W8 center was unambiguously proven by hyperfine satellites of isotopically ^{61}Ni-enriched HPHT diamonds [15]. Careful EPR studies on the W8 center revealed the $S = \frac{3}{2}$ spin state with ^{13}C hyperfine structure of four equivalent carbon atoms with no zero-field splitting and isotropic g factor in the EPR spectrum. These findings concluded a

*thiering.gergo@wigner.hu
†gali.adam@wigner.hu

T_d symmetry of the defect and led to the negatively charged Ni substitutional defect model Ni_s^-, which was supported by atomistic calculations [16–21]. Thus, the EPR center of Ni_s defect is well identified and not considered further in this study. We further note that the W8 EPR center is associated with the 2.51-eV absorption line [22–24] and the 2.56-eV photoluminescence (PL) [25,26] and optically detected magnetic resonance (ODMR) [25,26] centers.

Numerous other EPR, PL, and absorption centers were associated with the nickel impurity in diamond [2,3] but often with contradicting assignments based on tentative assumptions. According to previous *ab initio* calculations, the nickel interstitial has very high formation energy [27] (over 10 eV) with relatively low barrier energy (∼0.7 eV) [28] for diffusion, therefore, it is unlikely to appear in HPHT diamonds or Ni-contaminated diamonds after any thermal treatments. Depending on the position of the Fermi level in diamond, the Ni_s and NiV defects are the most stable forms of nickel impurity in diamond in the absence of other impurities [27]. As a consequence, the association of EPR and optical centers with Ni interstitials defects in diamond should be reconsidered and might be the fingerprint of NiV defects. Therefore, we briefly summarize those Ni-related EPR and optical centers below that were associated with Ni interstitial and NiV defects in diamond.

One of the most prominent fingerprints of Ni impurity in diamond is the 1.4-eV PL center. Collins and Spear [29] measured 3.3-meV splitting in absorption for the zero-phonon line (ZPL) at 1.4 eV, whereas 2.9-meV doublet was observed in the cathodoluminescence spectra, and they derived 2.5 ± 0.1 meV activation energy from Boltzmann temperature dependence of the intensity of the doublet peaks. The splitting was later observed in high-quality PL spectra and yielded at 2.8 ± 0.1 meV [30]. The 1.4-eV PL center was correlated with the NIRIM-2 EPR center in diamond [29,31,32]. The NIRIM-2 EPR center has $S = \frac{1}{2}$ electron spin with an axially symmetric $g_\parallel = 2.3285$, $g_\perp = 0$ gyromagnetic tensor [33]. The EPR center was tentatively assigned to the positively charged interstitial Ni defect [27,33–35]. The 1.4-eV optical center was also detected in magnetic circular dichroism of the optical absorption (MCDA) measurements [36]. Aside from the 1.4-eV signal, a 1.06-eV signal was also observed with sharing the same trigonal symmetry along the ⟨111⟩ axis.

Another clear optical signal in Ni-contaminated diamonds appears at 418 nm [37–39]. The 418-nm ZPL line splits into two individual lines at low temperatures (below 90 K) by 10 meV at 2.964 and 2.974 eV (Ref. [37]). We note that the excited state exhibits unusually long lifetime of 40 μs for $T \leqslant 15$ K temperatures that may indicate a forbidden optical transition. Furthermore, the 2.964-eV PL peak is found to be ODMR active [39] by applying 0.84 . . . 1.02 T external magnetic fields and 36 GHz microwave excitation under 325-nm illumination. Both the exceptionally long lifetime and the ODMR phenomena were associated with the existence of triplet levels between the singlet levels [37].

The NIRIM-5 EPR center was observed in boron-doped and Ni-contaminated diamonds [40–42] and this EPR center might be correlated with the 418-nm PL center [42]. We note that the NIRIM-5 EPR center [43] is identical to the NOL1 EPR center [40,41] in the literature. The NOL1/NIRIM-5 EPR center has $S = 1$ electron spin with an axially symmetric $g_\parallel = 2.0235$, $g_\perp = 2.002$ gyromagnetic tensor with the parallel direction along the ⟨111⟩ direction. Furthermore, they observed a zero-field splitting (D) at 170 GHz (0.707 meV) which they interpreted so that the $ms = \pm 1$ spin level has deeper energy than that of the $ms = 0$ spin level, i.e., the sign of the D is negative. The interpretation of the hyperfine satellite lines in the EPR spectrum varies in the literature: they were either tentatively attributed to ^{11}B isotopes with claiming a boron-nickel complex as the origin [42] or to the combination of ^{13}C and ^{61}Ni nuclear spins with claiming the NiV defect as the origin [41].

Recent experimental photocurrent measurements together with *ab initio* calculations in nickel-contaminated diamonds concluded that the photocurrent thresholds at around 1.2 eV [41,44] and 1.9 eV [7] are associated with the first and second acceptor levels of NiV defect [7]. The neutral NiV, NiV^0, is visible upon illumination of blue light in those diamond samples [7]. In that study, the NiV^0 was associated with the 1.22-eV absorption line [7] which is a bound exciton state with the hole split from the valence band. Furthermore, the NiV^0 was tentatively assigned to the NOL1/NIRIM-5 EPR center based on the calculated $S = 1$ ground state and ^{61}Ni and ^{13}C hyperfine constants. Boron doping is necessary to measure NiV^0 in dark by EPR because the Fermi level should be below $\sim(E_V + 1.25$ eV), where E_V is the valence band maximum of diamond.

Another fingerprint of Ni in diamond is the NE4 EPR center with $S = \frac{1}{2}$ electron spin [36,45]. It was proven [46] that NE4 EPR center is identical to AB1 EPR center [47–49] in the literature, and we use the NE4 label in the context. The g tensor ($g_\perp = 2.0923 \pm 0.0002$, $g_\parallel = 2.0027 \pm 0.0002$) of the NE4 center is anisotropic, which indicates an effective spin-orbit interaction. However, the hyperfine structure is unresolved for NE4, to the best of our knowledge. MCDA measurements clearly connected the NE4 EPR center to the 1.72-eV optical center [36]. The 1.72-eV absorption line splits to a doublet at 1.72- and 1.75-eV peaks where the latter is a vibronic level originating from the vibration of Ni atom [50]. These measurements also revealed a thermally activated spin-orbit fine structure with a splitting of 4.7 meV [50]. Tentative assignments for the origin of NE4 center are NiV^- (Refs. [27,51–53]) and Ni_s^+ (Ref. [36]). These assignments are clearly contradicting to previous assignment of the NiV defect to other EPR and/or optical centers.

Here we note that the assignment of NE4 EPR center to NiV defect was also driven from another argument in the literature. In HPHT diamonds with high nitrogen impurity concentration it was observed that consecutive annealing processes at ∼1800–1900 K [3] led to the series of EPR centers labeled by NE1-NE9 with reducing the EPR intensity of W8 and NE4 centers [3]. It was argued [1,50,51,54] that the process can be described by conversion of Ni_s^- (W8 EPR center) to NE4 EPR center by capturing a vacancy (NiV^- split nickel-vacancy defect) as the first step. Next, the six carbon dangling bonds near the NiV defect are replaced by respective one (NE7 EPR center), two (NE1 and NE5 EPR centers), three (NE2, NE3, and NE9 EPR centers), and four (NE8 EPR center) nitrogen atoms in the annealing stages, so the concentration of NE4 EPR center is greatly reduced in

the process. The NE1, NE5, NE2, NE3, NE9, and NE8 EPR centers were tentatively identified with using the number of observed ^{13}C and ^{14}N hyperfine lines in the spectra.

We further note that NE4* EPR center with $S = 1$ electron spin and isotropic $g = 2.0039(1)$ was reported [55]. In this EPR center, the zero-field splitting is $D = 35.8(1)$ mT (1.052 GHz or 3.89 μeV). A theoretical study associated the NE4* EPR center with NiV^0 (Ref. [27]) based on the relatively good agreement between the calculated (60 MHz) and observed (79 MHz) ^{13}C hyperfine splitting which contradicts to the assignment of NiV^0 to NOL1/NIRIM-5 EPR center [7]. We note that various PL centers with ZPL energies at 1.83, 1.92, 2.02, 2.1, and 2.2 eV were observed in the diamond samples where the NE4* EPR center was present [55]. We note that ^{61}Ni hyperfine satellites were not seen in EPR, thus, nickel presence in NE4* is not proven unambiguously in Ref. [55].

The brief summary of previous studies on Ni-related defects in diamond shows that NiV defect plays a crucial role in Ni-contaminated diamonds but there are conflicting interpretations about their fingerprints in the optical and electron paramagnetic resonance spectra. We apply here *ab initio* calculations to characterize the magneto-optical spectrum of NiV defect in diamond. We organize the paper by the following sections. First, we describe the theoretical method in Sec. II. Next, we show our *ab initio* results on the NiV center in Sec. III. We discuss our results in Sec. IV. We conclude in our study that the 1.4-eV PL center and the corresponding NIRIM-2 EPR center are associated with the NiV$^-$ defect. We show in Sec. IV D that NiV$^-$ can act as a qubit with favorable properties. Finally, we summarize our paper in Sec. V. The derivation of methodological advances as well as the discussion of the origin of the NE4 center is given in the Appendixes.

II. METHODOLOGY

We characterize the nickel-vacancy defects by plane-wave supercell calculations within spin-polarized density functional theory (DFT) as implemented in the VASP code [56]. We determine the electronic structure within Born-Oppenheimer approximation where the ions are treated as classical particles. By moving these ions into various positions, i.e., configurational coordinate, the adiabatic potential energy surface (APES) can be mapped, where the global energy minimum corresponds to a special position of ions, which is also called optimized geometry. The geometry corresponding to the global energy minimum of APES for a given electronic configuration can be found by minimizing the quantum mechanical forces acting on the ions where we set a threshold at 10^{-2} eV/Å.

We embed the NiV defect in a 512-atom diamond supercell and sample the Brillouin zone at the Γ point. We use the projector augmented-wave method (PAW) [57,58] as implemented in VASP. We use the standard PAW projector for carbon ions and such PAW projector for nickel ion which includes the $4p$ atomic orbitals as valence. We apply a cutoff of 370 eV for the plane-wave basis. We calculate the excited states with the constrained-occupation DFT method (ΔSCF method) [59]. Generally, we use the Heyd-Scuseria-Ernzerhof (HSE06) hybrid functional [60,61] which reproduces the experimental band gap and the charge transition levels in diamond or other group-IV semiconductors within 0.1 eV accuracy [62,63]. We use the charge correction as we described in Ref. [64] in Sec. III A which is based on Makov and Payne [65] with the correction from Lany and Zunger [66].

We employ the Huang-Rhys theory [67] to calculate the phonon sideband of the optical spectrum [4,68]. The phonons are calculated within the semilocal Perdew-Burke-Ernzerhof (PBE) [69] functional but the respective optimized geometry of the ground and excited states within HSE06 functional.

We determine the energy levels of the $e \otimes E$ Jahn-Teller system for NiV$^-$ in Sec. III C 1 by a numerical code implemented in GNU octave that we describe in Refs. [4,70]. Additionally, we use a similar code for the $(e \otimes e) \otimes E$ product Jahn-Teller system [71–73] to determine the fine polaronic structure of NiV^{2-} in Sec. III D.

The spin-orbit energies and the effective electron orbital moment within scalar-relativistic approximation and within the PAW sphere of all ions are calculated at fixed geometries as obtained from the spin-polarized geometry optimization calculations in VASP. The spin quantization axis is fixed along the trigonal symmetry axis of the defect.

We calculated the hyperfine coupling parameters between the nuclei and electrons spins as implemented in the VASP code [74]. It is highly important to obtain an accurate spin density around the core of the ions, therefore, the numerical parameters are adapted to this end. We applied an increased plane-wave cutoff of 600 eV in the hyperfine tensor calculations. Furthermore, the core polarization hyperfine terms from Ni core orbitals are significant [75], thus, we treated the Ni $3s$, $3p$, $4s$, $3d$, $4p$ orbitals as valence electrons (i.e., Ni_sv_GW PAW projector) and determined the spin polarization of $1s$, $2s$ as core orbitals. We included the core spin polarization in the Fermi contact term within the frozen valence approximation [76].

III. RESULTS

A. Electronic structure and possible charge states

The split-vacancy configuration and the electronic structure of nickel-vacancy defect are similar to those of silicon-vacancy and other group-IV impurity-vacancy complexes that have been recently analyzed in detail [4,77]. The commonality of these centers arises from the fact that the impurity ion sits at the inversion center of two adjacent vacancies with creating six carbon dangling bonds that provide the electrical, optical, and magnetic activities of the centers within D_{3d} symmetry. In NiV defect, the d orbitals play an additional role beside the carbon dangling bonds [27,53] that we summarize below.

The six-dimensional configuration space of the six carbon dangling bonds around the Ni atom gives rise to the following states in ascending energy order: $(a_{1g}^2\ a_{2u}^2\ e_g^4\ e_u^2)$, where g and u are the even- and odd-parity characters of the corresponding wave functions. The a_{1g}, a_{2u}, e_g orbitals are completely filled closed shells in the valence band. The remaining e_u orbital is occupied by two electrons in the neutral charge state that gives $S = 1$ spin for the system with $|^3A_{2g}\rangle$ multiplet state (see Fig. 1 for details).

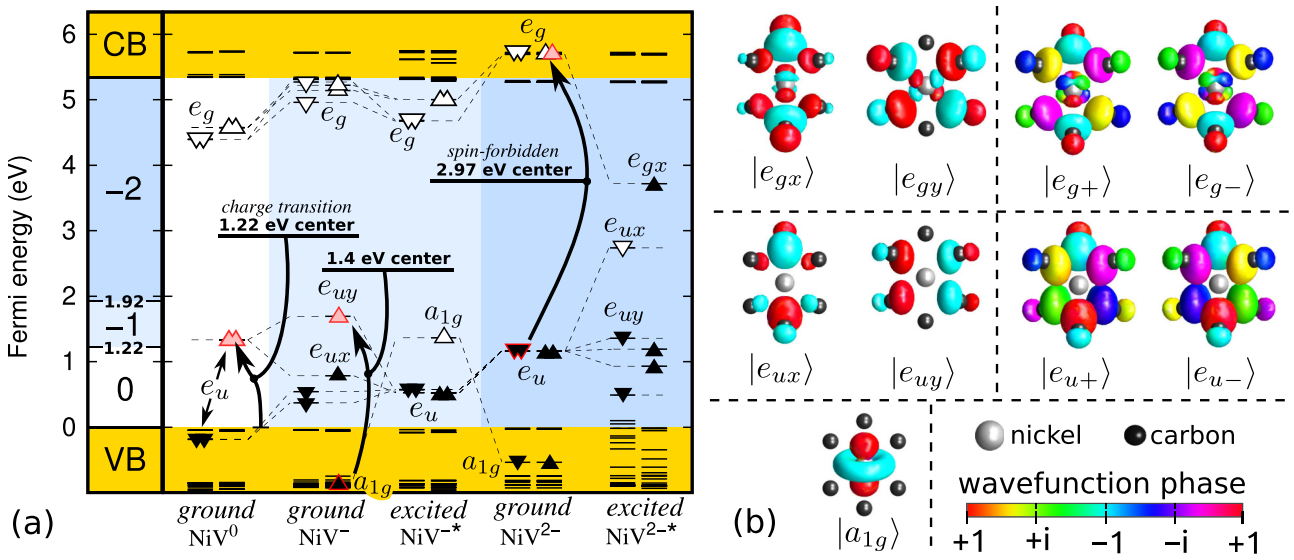

FIG. 1. (a) Kohn-Sham levels of neutral, negative, and doubly negative NiV defects near the band edges of diamond. We denote the *ab initio* charge transition levels on the left. We also denote the excitation process and the Kohn-Sham levels of optically excited NiV^- (1.4 eV) and NiV^{2-} (2.97 eV) centers. Additionally, we show photoionization process for NiV^0 defect (1.22 eV), where an electron at VBM (valence band maximum) is excited into the e_g level, thus transforming it into the NiV^- in the process. VB and CB correspond to valence band and conduction band, respectively. (b) Visualization of single-particle Kohn-Sham wave functions. The gray ball depicts the impurity atom, while the black balls depict the six first-neighbor carbon atoms. The real ($|e_x\rangle$, $|e_y\rangle$) degenerate orbitals can be transformed to the complex ($|e_+\rangle$, $|e_-\rangle$) combinations as $|e_\pm\rangle = \frac{1}{\sqrt{2}}[|e_x\rangle \pm i|e_y\rangle]$ (see details in Ref. [4]) to show the effective $L_z = \pm 1$ orbital moment of the wave functions. We note that the Ni $3d$ atomic orbitals significantly couples to $|e_g\rangle$ while $|e_u\rangle$ shows significant Ni $3p$ and $4p$ characters too. These Ni atomic orbitals are mainly responsible for the spin-orbit coupling in $|e_g\rangle$ and $|e_u\rangle$.

One might notice that there is an additional unoccupied e_g orbital at higher energy in Fig. 1(a). Nickel $3d$ atomic orbitals split to $a_{1g} \oplus e_g \oplus e_g$ levels in D_{3d} crystal field and they are allowed to mix with the e_g carbon dangling bond state. Consequently, the bonding e_g orbital is fully occupied and deeply confined in the valence band but the antibonding variant is resonant with the conduction band minimum (CBM) as we depict in Fig. 1(b).

The NiV defect in diamond exists in three different charge states as was previously found [7]. The $(0|-)$ charge transition occurs at $E_V + 1.22$ eV and the $(-|2-)$ is at $E_{VBM} + 1.92$ eV. We show the charge transition levels visually in Fig. 1(a).

We show the detailed results for NiV^0, NiV^-, and NiV^{2-}, respectively. We determine the spin-orbit-induced zero-field splitting tensor for the spin-triplet NiV^0 defect in Sec. III B 1 which identifies the corresponding NOL1/NIRIM-5 EPR center. The excitation energies between the localized states are also given in Sec. III B 2. The ground state of NiV^-, $|^2E_u\rangle$, is simultaneously Jahn-Teller and spin-orbit active (see Sec. III C 1 for details). We derive the anisotropic g factors directly from *ab initio* calculations for NiV^- in Sec. III C 2. According to our results, there is an optical excitation process between the $e_u \leftrightarrow a_{1g}$ orbitals, where the a_{1g} is strongly localized to the Ni $3d$ atomic orbital. Section III C 3 describes the results on this process. Additionally, we describe the results about the excitation pathways of NiV^{2-} defect in Sec. III D, where the excited state can be constructed by promoting an electron from the fully occupied e_u level to the empty antibonding e_g level resonant with the conduction band [see Fig. 1(a)].

B. NiV^0 defect

We provide a description about the ground and excited states of the neutral NiV defect where we apply a new theory in the calculation of the zero-field splitting (ZFS) going beyond the usual first-order perturbation theory.

1. Ground state and spin Hamiltonian

NiV^0 has $S = 1$ ground state as the e_u orbital occupied by two electrons in p-type diamond forming a $|^3A_{2g}\rangle$ ground state. In D_{3d} symmetry, the dipolar electron spin–electron spin interaction (D_{SS}) splits the $ms = 0$ and $ms = \pm 1$ levels with no external magnetic field, i.e., ZFS. Since the spin density is mostly localized on the carbon dangling bonds in third-neighbor distance the strength of this interaction is relatively small, about 0.89 GHz or 0.004 meV (see Ref. [7]). Spin-orbit interaction can also contribute to ZFS labeled as D_{LS}. We show below that the spin-orbit energy is in the order of meV for NiV defects, thus, it may significantly contribute to ZFS even in the second order. Next, we discuss this issue.

The magnitude of ZFS, D, can be described as $D = D_{SS} + D_{LS}$. In D_{3d} symmetry, the D has the following form:

$$\hat{D} = D\big(\hat{S}_z^2 - \tfrac{1}{3}S(S+1)\big), \tag{1}$$

resulting in a D energy gap between the $ms = \pm 1$ and 0 sublevels. If D is positive, then the $ms = \pm 1$ level is above that of $ms = 0$. We developed a theory and method to calculate the self-consistent total energy of the system in the $ms = \pm 1$ and 0 states, where the latter can be achieved by rotation of the unpaired electron spins by 90° in the spin-orbit calculations (see Appendix A). We emphasize that this methodology goes

beyond the usual first-order perturbation theory of the ZFS calculation because it allows for the relaxation of orbitals as a function of the spin state. We obtain $D = 0.73$ meV by this procedure. As the strength of D_{SS} is two orders of magnitude smaller, the ZFS should originate from spin-orbit interaction, which is discussed next.

As the effective angular moment of $^3A_{2g}$ state is zero, the spin-orbit interaction will not split the spin sublevels in the first order. In the second order, the $|\,^3A_{2g}\rangle$ can interact spin selectively with the higher level singlet states. In particular, $|\,^1E_g\rangle$ and $|\,^1A_{1g}\rangle$ singlet states exist from the $e_u^{(2)}$ electronic configuration, which is similar to the SiV^0 defect (see the Supplemental Material in Ref. [78]). The $ms = 0$ state of $|\,^3A_{2g}\rangle$ can only interact with $|\,^1A_{1g}\rangle$ (see Ref. [78]). By calculating the energy gap between these electronic states (Θ) and the spin-orbit coupling (λ_0), the perturbative approach yields the formula (see Appendix B)

$$D_{\mathrm{LS}}^{\mathrm{perb}} = \frac{\lambda_0^2}{\Theta}, \tag{2}$$

and $D_{\mathrm{LS}}^{\mathrm{perb}} = 0.79$ meV with $\Theta = 680$ meV and $\lambda_0 = 23.2$ meV which well explains the order of magnitude obtained by the fully self-consistent approach. Our derivation also highlights the importance of HSE06 functional because Θ is greatly underestimated by the PBE functional, which results in too large D constant in the self-consistent approach by PBE (see Appendix B).

Our results provide further strong evidence that the NOL1/NIMIR-5 EPR center is NiV^0 defect in which they derived $|D| = 0.707$ meV ZFS in the experiments [40,41], and NE4* EPR center can be clearly disregarded for the origin of NiV^0 which has three orders of magnitude smaller D constant. On the other hand, we propose a positive sign for the D constant in NOL1/NIRIM-5 EPR center which goes against the proposition in Refs. [40,41]. We provide further arguments for the identification in the Discussion section (Sec. IV A).

2. Excited states

We calculated the $^3A_{1g}$ to ^3E_u optical transition energy which results in 1.66 eV with 72.4 meV Jahn-Teller energy in the ^3E_u excited state. The ^3E_u excited state can be described as promoting an electron from a_{1g} level resonant with the valence band to the e_u level in the gap. This excitation energy is significantly larger than that of the calculated acceptor level at $E_V + 1.22$ eV, i.e., larger than the ionization threshold. The strong optical ZPL resonance at 1.22 eV in the absorption spectrum [7] should be associated with the bound exciton states where the NiV$^-$ defect loosely binds a hole split from the valence band maximum. Recently, such excited states have been identified in SiV^0 defect [79], where the calculation of optically active states and the corresponding levels is a highly challenging task (see Supplementary Materials in Ref. [79]), and it is beyond the scope of this study. The possible fingerprint of the optical excitation from the resonant defect state is discussed in Sec. IV A.

As we claimed in the previous section, $|\,^1E_g\rangle$ and $|\,^1A_{1g}\rangle$ singlet states occur too. Our HSE06 DFT calculations (see Appendix A and Ref. [80]) tentatively predict these levels at 0.21 and 0.68 eV above the triplet level. These states may play a role in the nonradiative decay process from the optically allowed excited states and the spin-flip process of the ground-state electron spin of NiV^0 defect [78].

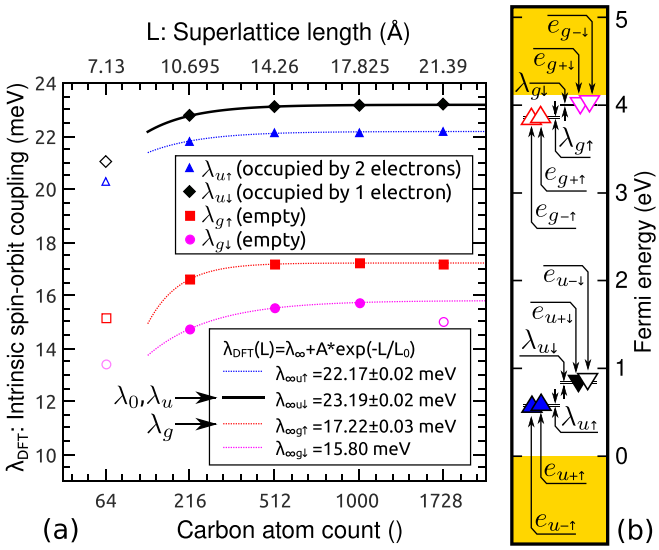

FIG. 2. (a) Supercell size (L) dependence of *ab initio* intrinsic spin-orbit coupling λ_0 (black curve) in NiV$^-$ (see Sec. III C 2 for details). We use the $\lambda_{g/u}$ parameters (black and red curves) to approximate the NiV^{2-} system (see Sec. III B 2 and Appendix C). (b) Kohn-Sham orbitals of NiV$^-$ system by means of PBE functional and applied spin-orbit coupling.

C. NiV$^-$ defect

We continue the investigation with the negatively charged NiV defect. We first discuss its electronic gound state, its effective spin Hamiltonian, and finally the optical excited state.

1. Spin-orbit coupling and electron-phonon coupling

Here we focus on the ^2E_u ground state. The ground state exhibits spin-orbit splitting according to our *ab initio* calculations. We note that the ^2E_u multiplet splits into two individual Kramers doublet in a double-group representation of D_{3d}. That is, the $(e_{u+}^{\uparrow}; e_{u-}^{\downarrow})$ spin orbitals with effective $J_z = \pm\frac{3}{2}$ total angular momentum exhibit higher total energy than that of the low moment $J_z = \pm\frac{1}{2}$ configurations $(e_{u+}^{\downarrow}; e_{u-}^{\uparrow})$ by the intrinsic λ_0 energy. We labeled here the respective spin-up and spin-down states by arrows. The splitting occurs at zero magnetic field. We computed the strength of intrinsic spin-orbit coupling with a procedure as described in our previous study [4], where we find little change in the calculated λ_0 as a function of supercell size (see Fig. 2) because of dominant and large spin-orbit field of the Ni ion.

The system exhibits $e_u \otimes E_g$ Jahn-Teller instability that reduces the observable zero-field splitting. The intrinsic λ_0 has to be multiplied by the Ham vibronic reduction factor p as we described in our previous work [4,70]. We solved the $e_u \otimes E_g$ Jahn-Teller–type electron-phonon Hamiltonian and obtained $p = 0.124$ Ham reduction factor by diagonalizing the following Hamiltonian up to 15-phonon

limit,

$$\hat{H} = \hbar\omega(a_X^\dagger a_X + a_Y^\dagger a_Y + 1) + F(\hat{X}\hat{\sigma}_z - \hat{Y}\hat{\sigma}_x) + G[(\hat{X}^2 - \hat{Y}^2)\hat{\sigma}_z + 2\hat{X}\hat{Y}\hat{\sigma}_x], \tag{3}$$

where the $\hat{X}, \hat{Y} = (a_{X,Y}^\dagger + a_{X,Y})/\sqrt{2}$ configurational coordinates (X, Y) describe a two-dimensional quantum harmonic oscillator with frequency ω. The F and G parameters describe the linear and quadratic orbital-vibronic interaction. We obtain the latter parameters from the equations of $E_{\rm JT} = \frac{F^2}{2(\hbar\omega_e - 2G)}$ and $\delta_{\rm JT} = \frac{4E_{\rm JT}G}{\hbar\omega_e + 2G}$ where $E_{\rm JT}$ and $\delta_{\rm JT}$ are the Jahn-Teller energy and barrier energy between the global energy minima of the calculated APES (see Refs. [4,70]).

The *ab initio* spin-orbit coupling $\lambda = p\lambda_0 = 2.88$ meV agrees well with the experimentally observed $\lambda_{\rm expt.} = 2.8 \pm 0.1$ meV splitting of the 1.4-eV optical center (see Table I for details) but more than a factor of 2 difference to the observed spin-orbit splitting of the 1.72-eV optical center (4.7 meV) associated with the NE4 EPR center. Since the accuracy of our calculations is much better than this (see Refs. [4,70]) our result implies that NiV^- is associated with the 1.4-eV optical center and not with the 1.72-eV optical center.

2. *Effective spin Hamiltonian for the ground state*

We derived the four-dimensional effective spin Hamiltonian for group-IV vacancy defects in our previous work [see Eq. (7) in Ref. [4]] that also applies for the ^2E_u ground state of NiV^-,

$$\hat{H}_{\rm eff} = \underbrace{-p\lambda_0}_{-\lambda}\hat{L}_z\hat{S}_z + \mu_B(g_S\hat{\boldsymbol{S}}\boldsymbol{B} + 2\delta_p g_L\hat{S}_z B_z + pg_L\hat{L}_z B_z), \tag{4}$$

where the $\hat{\boldsymbol{S}} = (\hat{S}_x, \hat{S}_y, \hat{S}_z)$ and $\hat{L}_z$ operators label the orbital angular moment ($L_z = \pm 1$) and spin ($S_z = \pm\frac{1}{2}$) and their respective interaction with the magnetic field, $\boldsymbol{B} = (B_x, B_y, B_z)$. We note that the negative sign of λ in Eq. (4) reflects that the $|E_{3/2}\rangle$ with total angular moment of Kramers doublet of $J_z = \pm\frac{3}{2}$ is energetically favorable over that of $|E_{1/2}\rangle$ with $J_z = \pm\frac{1}{2}$, in agreement with the third Hund's rule. Here, we define the parallel z direction as the symmetry axis of the defect ($\langle 111\rangle$ direction in diamond). $\mu_B = 0.057\,88$ meV/T is the Bohr magneton and $g_S = 2.002\,319$ is the g factor of the free electron. The orbital $g_L = 0.7821$ factor (or Stevens's reduction factor [81]) appears in Eq. (4) because the $L_z = \pm 1$ orbital moment in D_{3d} symmetry is only an effective angular momentum as there is no axial rotational symmetry. However, our present *ab initio* method cannot determine the orbital moment. Therefore, we used the experimentally known g_L factor of the e_u orbital in SiV^- (see Table III in Ref. [4]). The e_u orbitals of NiV^- and SiV^- are basically identical coming from the six carbon dangling bonds (cf. Fig. 1 of this paper and Fig. 8 in Ref. [4]), thus this approximation should be fairly valid. We note that the $\delta_p = 0.0839$ parameter in Eq. (4) is a second-order effect of Jahn-Teller interaction when the magnitude of spin-orbit coupling comparable or larger than that of the Jahn-Teller effect (see Ref. [4] for explanation).

The eigenenergies of the electron spin states under constant external magnetic field along the symmetry axis ($B_z \neq 0$, $B_x = B_y = 0$) can be expressed as

$$E_\parallel = \underbrace{\mu_B(g_S S_z + 2\delta_p g_L S_z + pg_L L_z)}_{g_\parallel S_z^{\rm eff}} B_z, \tag{5}$$

TABLE I. Fine-structure and EPR parameters of the NiV^0 and NiV^- defects and the corresponding *ab initio* data. We note that NE4* and NE4 centers were previously associated with NiV^0 and NiV^- defects too, thus, we provide here their EPR parameters for comparison.

NiV^0	$S = 1$	
Ab initio spin-spin ZFS	$D_{\rm SS}$	+0.004 meV
Ab initio spin-orbit ZFS	$D_{\rm LS}$	+0.73 meV
ZFS expt. (NOL1/NIRIM5)	$D_{\rm expt.}$	0.707 meV[a]
Expt. g tensor (NOL1/NIRIM5)	$g_\parallel$	2.0235[a]
Expt. g tensor (NOL1/NIRIM5)	$g_\perp$	2.002[a]
ZFS expt. (NE4*)	$D_{\rm expt.}$	3.89 μeV[b]
Expt. g tensor (NE4*)	$g_\parallel = g_\perp$	2.0039[b]
NiV^-	$S = \frac{1}{2}$	
Vibration energy	$\hbar\omega$	66.4 meV
Jahn-Teller energy	$E_{\rm JT}$	72.4 meV
Jahn-Teller barrier energy	$\delta_{\rm JT}$	2.4 meV
Ham vibronic reduction factor	p	0.124
Intrinsic spin-orbit coupling	λ_0	23.2 meV
Effective spin-orbit coupling	$\lambda = p\lambda_0$	2.88 meV
Expt. spin-orbit (NIRIM2, 1.4 eV)	$\lambda_{\rm expt.}$	2.8 ± 0.1 meV[c]
Steven's orbital reduction factor	g_L	0.7821[d]
Jahn-Teller second-order effect	δ_p	0.0839
Ab initio g tensor: $g_\parallel = g_S + pg_L + 2\delta_p g_L$[e]		2.33
Ab initio g tensor:	$g_\perp$	0
Expt. g tensor (NIRIM2, 1.4 eV)	$g_{\parallel\rm expt.}$	2.3285[f]
Expt. g tensor (NIRIM2, 1.4 eV)	$g_{\perp\rm expt.}$	0[f]
$Ni_sN_3^0$ (see Appendix D)	$S = 1/2$	
Expt. spin-orbit (NE4, 1.72 eV)	$\lambda_{\rm expt.}$	4.7 meV[g]
Ab initio g tensor: $g_\parallel = g_S + 2\langle\hat{L}_z\rangle$		2.0058
Ab initio g tensor: $g_\perp = g_S + 2\langle\hat{L}_\perp\rangle$		2.0942
Expt. g tensor (NE4, 1.72 eV)	$g_{\parallel\rm expt.}$	2.0027(2)[h]
Expt. g tensor (NE4, 1.72 eV)	$g_{\perp\rm expt.}$	2.0923(2)[h]

[a]Experimental data measured at 4 . . . 20 K in Ref. [40].
[b]Experimental data from Ref. [55]. The experimental data at $T = 4$ K is $D = 33.5$ mT that we converted to eV units with its isotropic $g = 2.0039$ factor.
[c]Experimental data from Ref. [88].
[d]See Table III in Ref. [4]. We used the g_L values of $|^3E_u\rangle$ optically excited states of $XV(-)$'s, where are $|e_u\rangle$ hole orbitals are almost identical to that of $NiV(-)$. See Fig. 1 3(b) and compare to the $|e_u\rangle$ orbital in Fig. 8(b) in Ref. [4].
[e]$g_S = 2.002\,319$ is the free-electron g factor.
[f]Experimental data from Ref. [33].
[g]Experimental data from Ref. [50].
[h]Experimental data from Ref. [46].

where S_z^{eff} effective spin inherits its $\pm\frac{1}{2}$ eigenvalues from the real S_z spin. L_z and S_z have the same sign for $|E_{3/2}\rangle$ Kramers doublet and opposite sign for $|E_{1/2}\rangle$.

It is important to recognize that $\lambda = 2.8$ meV is much larger than the Zeeman energy caused by the applied external magnetic fields ($B \ll 10$ T). As a consequence, the quantization axis of $\boldsymbol{S}$ is strongly aligned towards the symmetry axis of the defect, and the perpendicular component of $\boldsymbol{B}$ cannot alter the direction of the spin quantization axis in the first order, thus, $g_\perp \approx 0$. By combining Eqs. (4) and (5) and $g_\perp \approx 0$, the effective spin Hamiltonian reduces to

$$\hat{H}_{\text{eff}} = -\lambda \hat{L}_z \hat{S}_z + g_\parallel \hat{S}_z^{\text{eff}} B_z \tag{6}$$

with

$$g_\parallel = g_S + 2\delta_p g_L + 2p g_L. \tag{7}$$

By combining $p = 0.124$, $g_L = 0.7821$, $\delta_p = 0.0839$ parameters from theory, we predict $g_\parallel = 2.33$. The *ab initio* data can be directly compared to the observed g tensors of NIRIM-2 and NE4 EPR centers in Table I. The calculated $g_\parallel = 2.33$ agrees well the experimental data at $g_\parallel = 2.3285$ of NIRIM-2, and they both possess $g_\perp = 0$. However, the NE4 EPR parameters with isotropic g tensor is clearly inconsistent with those of NiV^- defect.

3. Excited state and PL spectrum

The $|e_u\rangle$ hole in NiV^- can be excited into the $|a_{1g}\rangle$ level with dominant Ni $3d$ contribution that resides resonantly in the valence band Fig. 1(a). We applied the ΔSCF method in order to calculate the excited state. The $|^2A_{1g}\rangle$ excited state is an orbital singlet, thus there is neither Jahn-Teller instability nor spin-orbit splitting in the excited state. This is in stark contrast to the excited state of SiV^- and similar group-IV impurity-vacancy complexes.

The calculated ZPL energy is 1.37 eV with using the zero-point energy of the APES of $|^2E_u\rangle$ [lowest-energy polaronic solution of Eq. (3)]. We note that the onsite (Coulomb) repulsion on $|a_{1g}\rangle$ is so large in the ground state of NiV^- [see Fig. 1(a)] that the $\sim$3 eV single-particle gap between the occupied $a_{1g}^{\uparrow}$ and empty $e_{uy}^{\uparrow}$ levels decreases to 1.37 eV as obtained by ΔSCF method. That is, the removal of an electron from $|a_{1g}\rangle$ releases the onsite energy, thus, the ZPL energy is much smaller than the energy gap between the occupied and empty Kohn-Sham levels in the ground-state electronic configuration. This leads to a change in the order of Kohn-Sham levels in the excited-state electronic configuration.

The contribution of the phonon sideband to the PL spectrum was calculated within the Huang-Rhys theory (see also Ref. [4]). The calculated ZPL energy and line shape of the phonon sideband agree well to those of the 1.4-eV PL center (see Fig. 3). This is in stark contrast to the 1.72-eV optical center associated with the NE4 EPR center, in which phonon replicas can be observed at $n \times 30$ meV with respect to ZPL peak, where n is an integer.

The calculated Huang-Rhys factor $S \approx 1.27$ at $T = 0$ K contains the contribution of the symmetry-breaking E_g phonon modes in the PL spectrum which corresponds to Debye-Waller factor at about 0.3. The radiative lifetime of the excited state can be calculated (Ref. [82]) as

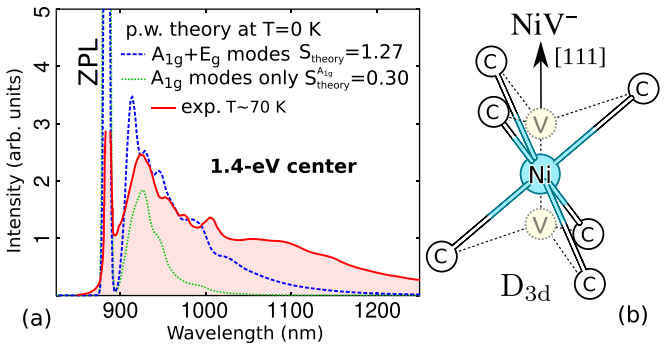

FIG. 3. (a) *Ab initio* PL spectrum of NiV^- optical defect within Huang-Rhys theory with taking into account only the symmetric (A_{1g}) and symmetry-breaking (E_g) phonons too. ZPL stands for the zero-phonon line where the theoretical ZPL was aligned to the experimental one at 1.4 eV for the sake of clarity in the comparison of the corresponding phonon sidebands. We applied 11.5-meV Gaussian broadening on the theoretical sideband and 4 meV on the ZPL. Experimental data of the 1.4-eV center is taken from Ref. [29]. (b) Sketch of nickel-vacancy defect exhibiting D_{3d} symmetry.

$$\tau_{\text{rad}} = \frac{3\pi\varepsilon_0}{n\omega^3|\mu|^2}, \tag{8}$$

where ε_0 is the dielectric constant of vacuum, $n = 2.42$ is the refraction index of diamond, $\hbar\omega$ is the excitation energy, and μ is the dipole integral between the ground and excited states. Specifically, the ground and excited states were represented by the e_u and a_{1g} orbitals in the transition dipole moment calculation, and $\hbar\omega = 1.4$ eV. Finally, we obtain $\tau_{\text{rad}} = 170$ ns. Experiments indicate that the PL lifetime of the 1.4-eV center is $\tau_{\text{expt.}} \sim 33$ ns (Ref. [83] as given in Ref. [29]). This implies that the nonradiative rate is competitive to the radiative one. The combination of these two effects is the experimentally observed lifetime that is the inverse of the sum of the two relaxation rates $\tau_{\text{expt.}}^{-1} = \tau_{\text{rad}}^{-1} + \tau_{\text{nonrad}}^{-1}$. Therefore, we estimate the inverse rate of nonradiative processes as $\tau_{\text{nonrad}} \sim 41$ ns.

D. NiV^{2-} defect

In the double-negative charge state, the e_u orbital is completely filled by four electrons. The corresponding ground state of NiV^{2-} is a totally symmetric $|^1A_{1g}\rangle$ singlet in D_{3d} symmetry, which is inactive in EPR measurements. However, it may be optically active. There is an unoccupied e_g orbital resonant with the conduction band to where an electron from the e_u level can be promoted [see Fig. 1(a)]. After the spin is flipped in the process, we arrive at the triplet states from $e_u e_g$ electronic configurations.

First, we start the analysis of the triplet excited states from $e_u e_g$ electronic configurations under D_{3d} symmetry. These have been thoroughly investigated for the case of SiV^0 defect [72], which shares the same triplet electronic configurations. Three electronic triplet states occur, $|^3A_{2u}\rangle$, $|^3E_u\rangle$, and $|^3A_{2u}\rangle$. These electronic configurations are separated by the electronic correlation energies of Ξ and Λ. Both e_u and e_g states are Jahn-Teller unstable caused by symmetry-distorting E_g phonons, therefore, a product Jahn-Teller effect occurs, alas,

$e_u \otimes e_g \otimes E_g$ Jahn-Teller system which heavily couples these electronic states [72]. The product Jahn-Teller effect results in two Jahn-Teller energy parameters $E_{\rm JT}^{(1)}$ and $E_{\rm JT}^{(2)}$, where $E_{\rm JT}^{(1)}$ is the constructive interference in the product Jahn-Teller effect, and is much larger [72,84] than the other parameter for the destructive interference. We indeed observed a large, 233-meV Jahn-Teller distortion energy in the triplet excited state by HSE06 Kohn-Sham ΔSCF calculation that we associate with $E_{\rm JT}^{(1)}$. The calculated energy gap between the ground state $|\,^1A_{1g}\rangle$ and triplet excited state is 2.87 eV.

In order to obtain the fine structure of triplet excited states, we solved the product Jahn-Teller Hamiltonian [see Eqs. (4)–(7) in Ref. [72]], which is

$$\hat{H} = \overbrace{\hbar\omega_E \sum_{\alpha}^{X,Y}\left(a_\alpha^\dagger a_\alpha + \frac{1}{2}\right)}^{\hat{H}_{\rm osc.}} + F\begin{bmatrix} 2\hat{X} & \hat{Y} & \hat{Y} & 0 \\ \hat{Y} & 0 & 0 & \hat{Y} \\ \hat{Y} & 0 & 0 & \hat{Y} \\ 0 & \hat{Y} & \hat{Y} & -2\hat{X} \end{bmatrix}, \quad (8)$$

where $F = \sqrt{\frac{1}{2}E_{\rm JT}^{(1)}\hbar\omega_E}$ is the linear Jahn-Teller coupling parameter and $\hbar\omega_E = 75.8$ meV is the energy of vibration mode with E symmetry. We note that the indices in the 4×4 matrix refer to the four-dimensional space spanned by the $|e_{uy}e_{gy}\rangle$, $|e_{ux}e_{gy}\rangle$, $|e_{uy}e_{gx}\rangle$, $|e_{ux}e_{gx}\rangle$ two-particle configurations. For the sake of simplicity, the Ξ and Λ electronic correlation parameters are neglected from Eq. (6) in Ref. [72]. Additionally, $E_{\rm JT}^{(2)}$ is also neglected. Thus, instead of two individual F_g, F_u parameters for e_g, e_u electronic orbitals, respectively, Eq. (8) contains only a single shared F parameter. Therefore, the present Eq. (8) above is much simpler than that of Eq. (7) in Ref. [72].

We note that the spin-orbit effect is largely quenched (e.g., Ref. [84]) and thus can be ignored in the fine-structure analysis. Finally, after numerical diagonalization up to 12-phonon limit, the polaronic $|^3\widetilde{A}_{2u}\rangle$ has the lowest energy followed by the polaronic $|^3\widetilde{E}_u\rangle$ which are separated by $\delta = 7.3$ meV.

According to our ΔSCF result, the Jahn-Teller distorted singlet level lies above the ground state's level by 3.33 eV, thus, the excited singlet level is above that of triplet by $\Delta E = 0.46$. Similarly to the triplet states the lowest-energy levels are the polaronic $|^1\widetilde{A}_{2u}\rangle$ and $|^1\widetilde{E}_u\rangle$ with energy spacing in the order of 10 meV. We note that this energy is very close to the predicted ionization threshold energy at ∼3.42 eV which is a photoionization process from the e_u orbital to the conduction bands with converting NiV^{2-} to NiV^-.

We determined the SOC parameters within the PBE level in the negative charge state. We inherited the λ_0 coupling parameter that of Fig. 2 for the e_u orbital: $\lambda_u = -\lambda_0 = -23.2$ meV. Additionally, we approximated the $\lambda_g = 17.2$ meV parameter for e_g orbital by taking the energy difference between $|e_{g+\uparrow}\rangle$ and $|e_{g-\uparrow}\rangle$ single-particle levels in the NiV^- system. By using the second-order perturbation theory, one can estimate the singlet inmixture to the triplet state by $c^2 \approx \frac{|\lambda_g|+|\lambda_u|}{2\Delta E} \sim 0.19\%$ (see Appendix C for details). However, second-order perturbation theory may be not accurate because the electron-phonon coupling and the spin-orbit coupling strengths are similar. Therefore, we incorporated the spin-orbit Hamiltonian into the Jahn-Teller Hamiltonian by including Eq. (C3) in Eq. (9) as proposed in Ref. [84]. We find that the $m_S = 0$ substates of $|^3\widetilde{A}_{2u}\rangle$ and $|^3\widetilde{E}_u\rangle$ polaronic states gain the same $c^2 \approx 0.025\%$ singlet character after numerical diagonalization of the electron spin-orbit-phonon Hamiltonian. We note that the formerly spin-forbidden transition becomes partially allowed due to inmixture of $|^1E_u\rangle$ singlet by perpendicular polarization of the emitted photons.

We conclude that the 418-nm (2.964-eV) PL center can be associated with the optical properties of NiV^{2-}. That PL center has extremely long lifetime 43 ± 3 μs below 15 K which implies a phosphorescence process [37]. Our results indicate that this process is the $|^3\widetilde{A}_{2u}\rangle \rightarrow |\,^1A_{1g}\rangle$ optical transition which is allowed by the slight inmixture of the singlet characters into $|^3\widetilde{A}_{2u}\rangle$. To estimate the radiative lifetime, one can apply Eq. (8) with dipole integrals between $e_u \leftrightarrow e_g$ localized orbitals for NiV^{2-} [cf. Fig. 1(a)] divided by c^2 responsible for the singlet character in the excited state. We obtain $\mu = 5.7$ Debye/c^2 which results in $\tau \approx 2.96\,\text{ns}/c^2 = 11.8\,\mu$s radiative lifetime. We note here that we still did not take into account the threefold degeneracy of the triplet excited state but 11.8 μs refers only to the bright $ms = 0$ state. If all the three $m_S = \pm 1, 0$ spin substates of the polaronic $|^3\widetilde{A}_{2u}\rangle$ are equally occupied at the given temperature, then the aforementioned lifetime has to be multiplied by 3 because no emission is expected from the dark $m_S = \pm 1$ states. The final deduced radiative lifetime at 35.5 μs approaches well the experimental data.

Furthermore, the doublet feature in the PL spectrum with energy gap of 10 meV can be explained by the polaronic gap between $|^3\widetilde{A}_{2u}\rangle$ and $|^3\widetilde{E}_u\rangle$. Additionally, the large ionic relaxation in the triplet excited state, i.e., $E_{\rm JT}^{(1)}$, explains the broad phonon sideband in the phosphorescence spectrum. We determine the PL sideband by means of Huang-Rhys theory in Fig. 4(a). We simulate the Huang-Rhys theory between the geometries of the ground state and the C_{2h} distorted excited triplet. Interestingly, the HSE06 optimized atomic positions seem to overestimate the experimental PL sideband and its S factor but the PBE functional seems to resemble it almost perfectly.

We also note that the absorption is only effective once the threshold energy of singlet excitations has been achieved. The calculated threshold energy is about 3.33 eV and it is very close to the photoionization threshold (∼3.42 eV). The optically active e_u levels reside inside the conduction band close to the conduction band minimum [cf. Fig. 4(c)], where the $e_u \leftrightarrow e_g$ transition is broadly split due to resonant conduction band states. As a consequence, we propose that narrow ZPL for absorption at 3.33 eV does not occur but a broad feature merging into the ionization band of the defect. We determine the photoluminescence excitation (PLE) spectrum in Fig. 4(b) by means of Huang-Rhys theory with the same parameters that we used for the photoluminescence. We further smear the spectrum with the calculated imaginary dielectric function associated with the electronic part of the ionization band as shown in Fig. 4(c).

We note that once the NiV^{2-} was ionized to NiV^- by ultraviolet illumination (∼3.42 eV) the same photon will reionize it to NiV^{2-} again. Furthermore, the calculated spin-orbit coupling is strong, thus, a very fast intersystem crossing rate can be assumed between the singlet and triplet states. As a

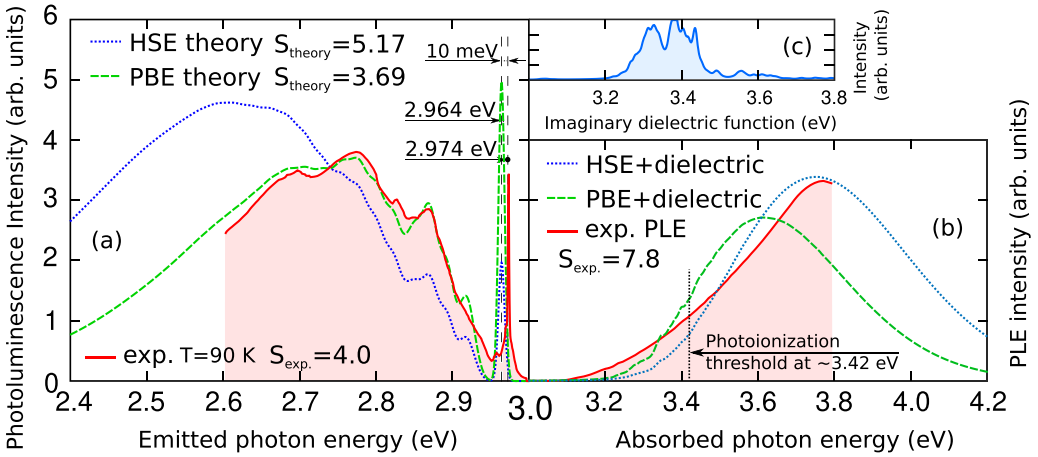

FIG. 4. (a) Theoretically predicted PL sideband of the NiV^{2-} by means of Huang-Rhys theory. We aligned the theoretical ZPL energy at 2.87 eV to the observed one at 2.964 eV, for the sake of sideband comparison. (b) Theoretically predicted PLE spectra for the 2.964-eV PL center. We obtained the PLE spectra by the following procedure. First, we convoluted the phonon sideband within Huang-Rhys theory with the imaginary dielectric function. Then, we aligned the mean value of this spectrum to the ΔSCF ZPL energy for the singlet transition at 3.33 eV. (c) Imaginary part of the dielectric function at the ground state of NiV^{2-} by means of DFT PBE calculations with $4 \times 4 \times 4$ k-point sampling within the Monkhorst-Pack scheme [85]. The experimental PL and PLE spectra of 2.97-eV center are taken from Ref. [37]. The theoretical curves (green and blue) are scaled to exhibit the same area under the curve as that of the red colored area of experimental spectra.

consequence, the photoluminescence excitation (PLE) spectrum of NiV^{2-} should be only visible upon illumination towards the singlet states with different characteristics compared to the phosphorescence spectrum. This conclusion is in accord to the experimental findings about the 418-nm phosphorescence center in which the PLE spectrum significantly differs from the phosphorescence spectrum where the PLE effect is visible with illumination energy larger than ∼3.2 eV [37].

IV. DISCUSSION

In this section we discuss the consequences of our *ab initio* results on NiV defects in the light of previous experimental data. In particular, some of the EPR and optical centers could be conclusively identified by NiV defects.

A. Origin of NOL1/NIRIM-5 EPR center and the 1.22-eV absorption center

We found in the self-consistent spin-orbit calculations of NiV^0 defect that ZFS parameter $D = +0.73$ meV of the ground state which agrees well with the experimental data of $|D| = 0.707$ meV of the NOL1/NIRIM-5 EPR center [40,41]. This result further supports our previous tentative assignment of NiV^0 to this center based on the calculated hyperfine signatures of ^{61}Ni and neighbor ^{13}C nuclear spins [7]. We discuss here the EPR parameters of the NOL1/NIRIM-5 EPR center and the previous models in detail.

The EPR measurement of the NOL1/NIRIM-5 EPR center with $S = 1$ spin is not trivial because of the giant ZFS parameter which would require too large external magnetic fields for direct measurement of the $\Delta ms = \pm 1$ transitions. Instead, the second-order $\Delta ms = \pm 2$ transitions could be detected by splitting the $S_z = \pm 1$ manifold under external constant magnetic fields [40,41]. It was concluded that the value of the D is negative, i.e., the $S_z = 0$ level lies above the $S_z = \pm 1$ levels because the EPR intensity did not show a strong temperature dependence (not shown) by lowering the measurement temperature from 20 to 4 K [41]. However, our result clearly implies that the value of D is positive. We find that the occupation number of the upper $S_z = \pm 1$ level is 0.21 and 0.57 at 4 and 20 K, respectively, thus, the EPR signal should be clearly detectable at 4 K and it does not radically increase with raising the temperature to 20 K. We think that the positive D value does not contradict with the experimental data. We note that the ZFS parameter D of the NE4* EPR center is 3.89 μeV that is orders of magnitude smaller than that of NOL1/NIRIM-5 EPR center. We found that the spin-orbit interaction is strong in the presence of Ni defect with axial symmetry, e.g., NiV^0, thus either the spin density is not localized on nickel impurity in NE4* EPR center or it is not related to nickel impurity at all.

The chemical structure of the defect can be often identified by the satellite hyperfine lines in the EPR spectrum which provide a direct fingerprint about the atom types in the core of the defect. However, the NOL1/NIRIM-5 EPR center is observed by the second-order $\Delta ms = \pm 2$ transition which makes the interpretation of hyperfine satellite lines ambiguous. For instance, the angular dependence of the ^{61}Ni hyperfine signal could not be monitored in the experiments, and the $A_{yy} \approx 20$ MHz component could be deduced. The calculated $A_{yy} = 25$ MHz by HSE06 DFT in our previous study agrees well with the experimental data. The other hyperfine satellites attributed to the ^{11}B nuclear spins in an EPR study [42] were not confirmed by a later EPR study [41] but they rather interpreted the hyperfine signals as isotropic hyperfine interaction with six nearest-neighbor ^{13}C nuclear spins of about 42.5 ± 5.7 MHz. Our previous *ab initio* results imply [7] that this is rather the A_{yy} component of ^{13}C nuclear spins (39 MHz in the calculation) but the $A_{zz} = 84$ MHz component is significantly larger. We conclude that the presence of boron

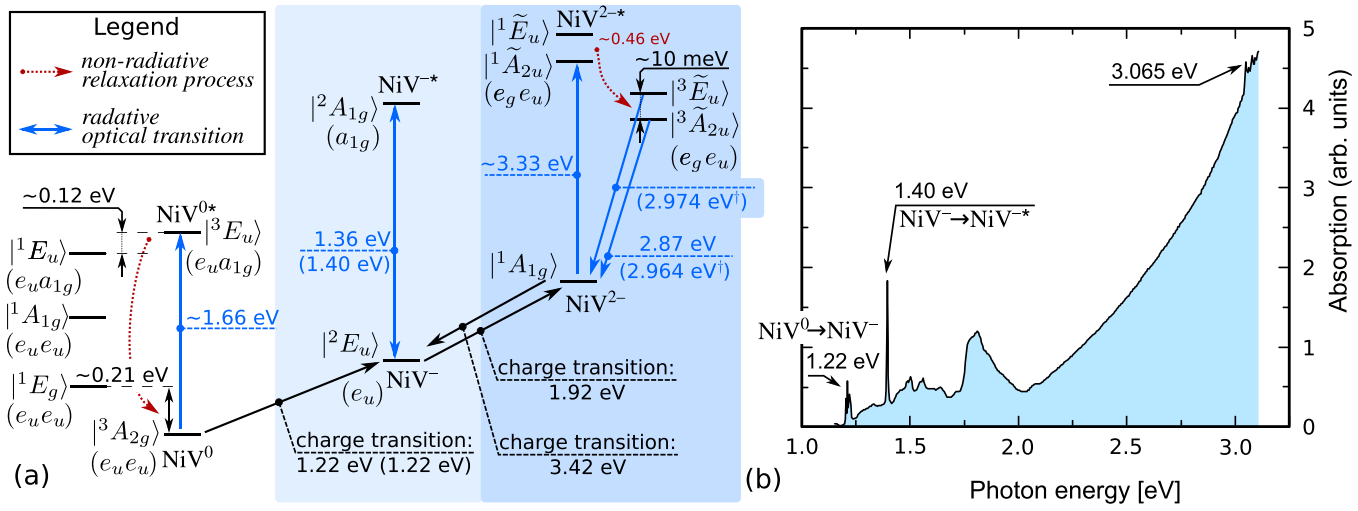

FIG. 5. (a) Many-electron states of NiV. The excitation energies inside the parentheses are experimental data (see Table I and the main text for details and interpretation). (b) Optical absorption spectra of low-nitrogen-concentration diamond taken from Ref. [44].

in the EPR center was not conclusively identified in the experiments, and the EPR hyperfine satellites of NOL1/NIRIM-5 EPR center can be naturally explained by the NiV^0 model.

The NOL1/NIRIM-5 EPR center is associated with the 1.22-eV absorption center [7,41,44]. The sharp lines in the 1.22-eV absorption spectrum are Rydberg bound exciton states of NiV^0. In the absorption spectrum beside the sharp lines, there is a broad feature between ≈1.75 and 2.00 eV [see Fig. 5(b)]. In this context, we note that a resonant a_{1g} level occurs in the valence band [see Fig. 1(a)]. Promoting an electron from the resonant a_{1g} state to the e_u defect level results in $|{}^3E_u\rangle$ excited state. The calculated ZPL energy is at ≈1.66 eV. We learned from previous PLE studies on silicon vacancy and related color centers in diamond that a broad band can be developed upon high-energy excitation which involves resonant states in the valence band with resulting a very broad absorption band [86,87]. We tentatively associate the broad band in the absorption spectrum in Ni-contaminated diamonds with the high-energy excitation of NiV^0.

B. Origin of the NIRIM-2 EPR center and the 1.4-eV optical center

Previous studies imply [88] that NIRIM-2 EPR center [33] and the 1.4-eV optical center [88] are correlated. Our results indicate that the magneto-optical parameters of the NiV^- defect appear in these EPR and optical spectra.

In particular, the ground state has an $|{}^2E_u\rangle$ character. The orbital doublet provides an effective $L_z = \pm 1$ orbital moment which leads to an effective spin-orbit splitting partially quenched by the dynamic Jahn-Teller interaction. In the double-group notation, this is a 4× degenerate state which splits to $|E_{u\frac{3}{2}}\rangle$ ($\Gamma^-_{5,6}$) and $|E_{u\frac{1}{2}}\rangle$ (Γ^-_4) 2× degenerate states [89,90]. Due to the presence of the orbitals of the relatively heavy element Ni ion in the spin-orbit interaction, the quenched spin-orbit gap will be relatively large (≈2.9 meV) which results in an effective $g_\perp \approx 0$ and $g_\parallel = 2.33$ when the external magnetic fields are orders of magnitude smaller than the spin-orbit gap. The calculated spin Hamiltonian parameters agree well with the experimental data (see Table I).

We found that the excited state of NiV^- defect is an orbital singlet. As a consequence, a doublet ZPL feature should appear in the fluorescence spectrum which is separated by the spin-orbit gap in the ground state. Indeed, 2.8 ± 0.1 meV splitting was observed in the 1.4-eV Ni-related optical center in diamond [88] which is close to the calculated parameter (2.88 meV, cf. Table I). The calculated ZPL energy (1.36 eV) and the line shape of the phonon sideband agree well with the experimental data (cf. Fig. 3).

We conclude that the NIRIM-2 EPR center and the 1.4-eV optical center are the fingerprints of the NiV^- defect in diamond. As a consequence, the tentative association of these centers with the Ni_i^+ defect [27,88] is not supported by our study. We believe that our proposal is consistent with the calculated formation energies of the defects, which is much higher for interstitial nickel defect than that for NiV defects [27], and also the calculated thermal stability of the nickel interstitial defect, which is relatively low because of the low barrier energy for diffusion [28]. In particular, the low barrier energy for diffusion of the Ni_i^+ defect is inconsistent with the relatively high thermal stability of the 1.4-eV optical center.

We note that the NE4 EPR center and the associated 1.72-eV optical center were tentatively associated with the NiV^- defect in the literature [1,3,27,51,52]. Obviously, our proposal for the origin of the NIRIM-2 EPR center and the associated 1.4-eV PL center as NiV^- defect suggests that the microscopic structure of the NE4 EPR center should be another Ni-related defect. This issue is discussed in Appendix D in detail supported by additional *ab initio* calculations.

C. Overview of NiV-related EPR and optical centers from theory

In our previous study, we identified the 1.22-eV and 1.92-eV photocurrent centers observed at room temperature as the first and second acceptor photoionization levels of NiV defect, respectively (see Ref. [7] and Fig. 1). The 1.22-eV absorption center observed at cryogenic temperatures is intimately related to the first photocurrent center as that is the Rydberg

TABLE II. Electronic excitation processes of NiV defect. We show the *ab initio* and experimental ZPL data if available. We also show the excitation processes which involve charge transitions.

Ground state	↔	Excited state	Theory	Expt.
$NiV^0(^3A_{2g})$	↔	$NiV^0(^3E)$	1.66 eV	
NiV^0	↔	NiV^{2-} + hole$^+$	1.22 eV	1.22 eV
$NiV^-(^2E_g)$	↔	$NiV^-(^2A_{1g})$	1.36 eV	1.40 eV
NiV^-	↔	NiV^{2-} + hole$^+$	1.92 eV	
$NiV^{2-}(^1A_{1g})$	↔	$NiV^{2-}(^1A_{2u})$	3.33 eV	
$NiV^{2-}(^1A_{1g})$	↔	$NiV^{2-}(^3A_{2u})$	2.87 eV	2.97 eV

bound exciton excited state below the ionization threshold of the NiV^0 defect. The associated NOL1/NIRIM-5 EPR center is conclusively identified as NiV^0 by the calculated ZFS parameter caused by the second-order spin-orbit interaction.

NiV^- defect is conclusively identified as the 1.4-eV optical center and the associated NIRIM-2 EPR center. The identification is based on the excellent agreement between the observed and calculated spin-orbit splitting of the ground-state levels, the g tensor of the ground-state spin, and the PL spectrum (see Tables I and II).

Additionally, our results suggest that NiV^{2-} defect is identified as the 418-nm (2.964-eV) phosphorescence center (see Table II) based on the calculated ZPL energy and the fine vibronic structure (see Fig. 4) of the excited state. The orders of magnitude of the radiative lifetime of the optical transition agreed well with the experimental data. The ground state of the defect is a spin singlet, therefore, it is nonparamagnetic and nonobservable by EPR spectroscopy.

The interpretation of the optical signals are summarized in Fig. 5. Our results explain previous reports on the photophysical properties of Ni-related optical centers. Under illumination above ∼2 eV, NiV^0 or NiV^- will be ionized to NiV^{2-}, and further absorption of ultraviolet photons will lead to phosphorescense from NiV^{2-}. Therefore, we suggest reinvestigation of diamond samples featuring 1.22- and 1.4-eV optical centers that the 418-nm optical peak may be activated by ultraviolet illumination.

D. Quantum optics protocols for NiV^-

In the present section, we will propose quantum optics protocols for the NiV^- defect spins which are similar to that of SiV^- defect spin [91–93]. A complete qubit control requires the following: (i) qubit initialization, (ii) coherent manipulation in the full Bloch sphere, (iii) readout of the qubit state.

First, we discuss the viability of orbital degree of freedom manipulation in the $|^2E_u\rangle$ ground state. That is, one may utilize qubit operations by coherently entangling the $|E_{u\frac{3}{2}}\rangle$ and $|E_{u\frac{1}{2}}\rangle$ Kramers doublets [cf. Fig. 6(a)]. One may (i) initialize the qubit states by cooling the system below 4 K that thermally quenches the upper state. However, the coherent manipulation is severely limited by the orbital relaxation time. According to Eq. (5) in Ref. [94], the orbital relaxation rates γ_+ and γ_- drive the transitions between the Kramers doublets as

$$\gamma_+ = 2\pi\chi\varrho\lambda^3 n(\lambda, T),$$
$$\gamma_- = 2\pi\chi\varrho\lambda^3 (n(\lambda, T) + 1), \quad (9)$$

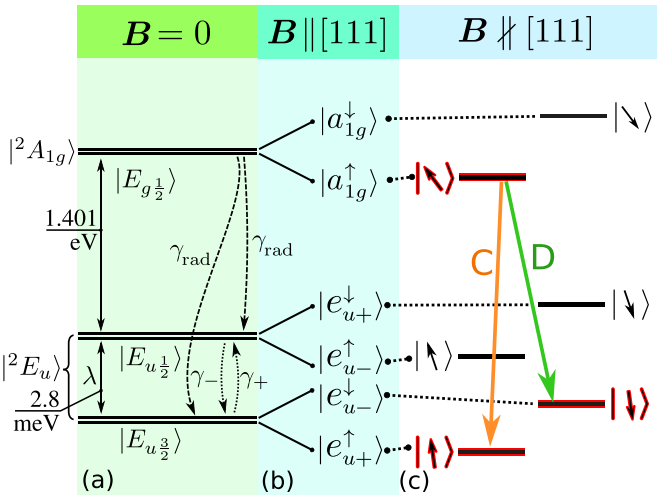

FIG. 6. Proposed quantum optics protocol for NiV^-. (a) At zero magnetic field the $|^2E_u\rangle$ ground state is split by λ into Γ_4 and $\Gamma_5 \oplus \Gamma_6$ spin-orbit sublevels [89]. (b) If one applies magnetic field along the z [111] axis, the Kramers doublets split. We label the individual levels by their $S_z = \{\uparrow, \downarrow\}$ spin and $L_z = \pm 1$ orbital moment by $|e^{\uparrow,\downarrow}_{u\pm}\rangle$ labels. (c) If the magnetic field is misaligned from the C_3 rotation axis, the spin projections will disorient from the $\boldsymbol{B}$ field direction according to Eq. (4). That is, the spin-orbit coupling does not allow the spin to fully align towards the $\boldsymbol{B}$ field, thus, optical transitions "D" will be optically active. We note that the $|a_{1g}\rangle$ orbital does not possess L_z angular moment, thus, its spin perfectly follows the magnetic field direction.

where λ is the splitting between the Kramers doublets and $n(\lambda, T)$ is the Bose-Einstein occupation of a phonon mode with λ energy at T temperature. The parameters χ and ϱ are constants related to average electron-phonon coupling strength and phonon density of states, respectively. In order to estimate the rates of NiV^-, we used the parameters as derived from the observed rates for SiV^- of which defect exhibits similar Jahn-Teller energy and vibration frequency [4]. Consequently, we assume that the $\chi\varrho$ product is the same for both systems. At high temperatures ($T \gg \hbar\lambda/k_B$ with k_B Boltzmann constant), thermal equilibrium can be assumed, thus, the orbital relaxation rate goes as

$$\gamma_+ \approx \gamma_- \approx \frac{2\pi}{\hbar}\chi\varrho\lambda^2 k_B T. \quad (10)$$

For the case of SiV^-, the experimentally observed homogeneous linewidth of photoluminescence spectra according to Fig. 2 in Ref. [94] follows $\gamma_\pm \approx 24.26\frac{\text{MHz}}{\text{K}}T$ expression. Additionally, the spin-orbit splitting is $\lambda = 258$ GHz [95] for the optically excited state of SiV^-. Finally, we deduce the $\chi\varrho$ parameter as $1.058 \times 10^{-28} s^2$ that we can use for NiV^-. On the other hand, NiV^- exhibits a large $\lambda = 2.8$ meV, thus, the opposite ($T \ll \hbar\lambda/k_B$) limit of Eq. (10) is required at ∼4 K,

$$\gamma_+ \approx 2\pi\chi\varrho\lambda^3 \exp\left(-\frac{\hbar\lambda}{k_B T}\right),$$
$$\gamma_- \approx 2\pi\chi\varrho\lambda^3. \quad (11)$$

One may note that acoustic phonons in γ_+ are exponentially quenched but the nonradiative relaxation γ_- process is present

even at $T = 0$ K thanks to spontaneous decay. Finally, amalgamating the deduced $\chi\varrho$ and observed λ parameters for NiV^-, we estimate the lifetime of $|E_{u\frac{1}{2}}\rangle$ at $1/\gamma_- = 29$ ps or less at elevated temperatures. However, the picosecond timescale is inadequate for coherent manipulation or readout procedure when the qubit information is encoded into the orbital degrees of freedom. One would need at least approach nanosecond regime [91,92,96]. Thus, we discuss the feasibility of spin degrees of freedom for the qubit operations in the context.

The qubit protocol for spins would require an additional magnetic field that would split the Kramers doublets. If one applies magnetic field disoriented from the defect's symmetry axis, then the formerly spin-forbidden transitions will be partially allowed [95]. Therefore, even the originally spin-forbidden transition "D" in Fig. 6(c) would be active for all optical manipulations. First, we discuss the qubit initialization process (i). The system can be cooled down below 10 K that thermally quenches the upper $|E_{u\frac{1}{2}}\rangle$ Kramers doublet. However, the Zeeman energy is inadequate to induce thermal quenching. Thus, one may optically pump transition "D" by a resonant laser that empties the $|e^{\downarrow}_{u-}\rangle$ state because transition "C" is off resonant in the process.

The coherent manipulation (ii) can be done by exciting the 1.401-eV transition by a highly redshifted detuned Raman laser pulse that coherently excites both spin states of $|E_{u\frac{3}{2}}\rangle$ (see Fig. 4 in Ref. [91]). (iii) Finally the readout can be utilized by the same resonant laser used for pumping. That is, an emitted photon can be detected only if the system was in the $|e^{\downarrow}_{u-}\rangle$ state before the readout pulse.

The electronic structure of NiV^- enables an all-optical technique for (i) initialization, (ii) coherent manipulation, and (iii) readout of the NiV^- qubit. This scheme utilizes the significantly longer spin coherence time that can be approximated by the $\tau_{\text{spin}} = 1/\gamma_+ \approx 99$ ns orbital transition rate (see Ref. [94] and the Supplemental Material in Ref. [97]) of Eq. (11) at 4 K. We note that the coherence time of the electron spin could be further limited by the neighbor nuclear spins [93,98,99]. The calculated $\approx$0.1 μs coherence time of NiV^- qubit at 4 K is significantly favorable over that of SiV^-. At 2 K, which is a technologically readily accessible operation temperature, the estimated lifetime is 0.73 μs for NiV^- qubit which makes it possible to carry out quantum information processing between the electron spin and a ^{13}C nuclear spin qubit in diamond (e.g., Ref. [100]). The defect exhibits inversion symmetry which prohibits direct coupling to stray electric fields, thus indistinguishable solid-state single-photon source can be realized. The ZPL wavelength of NiV^- can be efficiently converted to telecom wavelengths, and the contribution of coherent ZPL emission from the total emission is significant in the defect. This makes NiV^- defect spin to be an attractive system for quantum communication applications.

We reiterate here that the photocurrent signal of NiV^- has been recently identified at about 1.92 eV which is the second acceptor level of NiV defect with respect to the valence band [7]. Below the photoionization band, bound exciton excited states exist as the double negatively charged NiV can Coulombically bind a hole split from the valence band where the lowest-energy excited state has A_{1g} symmetry (see the symmetry analysis in the Supplemental Material of Ref. [79]). The presence of A_{1g} bound exciton state at $\sim$1.9 eV provides an alternative route for all-optical coherent manipulation where the excitation energy is $\sim$1.9 eV. We assume that because the energy gap between the bound exciton level at $\sim$1.9 eV and the lowest-energy excited level at 1.4 eV is relatively small, therefore, the nonradiative decay from the $\sim$1.9-eV state towards the 1.4-eV state is strong. As a consequence, the $\sim$1.9-eV resonant excitation may lead to an emission at 1.4 eV and below.

Another aspect of the photocurrent signal of NiV^- is the electrical readout of the qubit state. By using a high-power laser to drive optical transitions as depicted in Fig. 6, the nonlinear effects may lead to a two-photon absorption via the excited state. Since the optical transition "D" is resonant, the photocurrent signal may occur for a given qubit state, so photocurrent-based readout of the qubit state is doable.

V. SUMMARY

We addressed and determined the strength of spin-orbit and electron-phonon interactions for split-vacancy NiV defect in diamond which define its spectroscopical fingerprints. We unambiguously identified NiV^0, NiV^-, and NiV^{2-} related optical (EPR) centers in diamond as 1.22-eV (NOL1/NIRIM-5), 1.4-eV (NIRIM-2), and 2.964-eV centers, respectively. After identification of NiV color center in diamond, we show that NiV^- defect is a promising candidate to realize spin-to-photon interface and may be isolated as single defects to form quantum bits in diamond. NiV^- color center has relatively long electron spin coherence times with optical transition in the near-infrared wavelength region and exhibit minor spectral diffusion inherited through the inversion-symmetric structure of the defect. Furthermore, the NiV^- qubit can be also read out electrically. In p-type diamond, NiV^0 is a potential qubit with presumably long electron spin-lattice relaxation and spin coherence times similarly to the isovalent SiV^0 color center in diamond.

ACKNOWLEDGMENTS

A.G. acknowledges support from the National Research Development and Innovation Office of Hungary within the Quantum Technology National Excellence Program (Project Contract No. 2017-1.2.1-NKP-2017-00001) and the National Excellence Program (Project No. KKP129866) and the Quantum Information National Laboratory sponsored via the Ministry of Innovation and Technology of Hungary, and the European Commission of H2020 ASTERIQS project (Grant No. 820394). We thank the National Information Infrastructure Development Program for the high-performance computing resources in Hungary. G.T. was supported by the János Bolyai Research Scholarship of the Hungarian Academy of Sciences and the ÚNKP-20-5 New National Excellence Program for Ministry Innovation and Technology from the source of the National Research, Development and Innovation Fund. We acknowledge the high-performance computational resources provided by KIFÜ (Governmental Agency for IT Development) institute of Hungary as well as the DECI resource Eagle HPC based in Poland at Poznan with support from the PRACE aisbl.

APPENDIX A: SELF-CONSISTENT *AB INITIO* METHOD TO DETERMINE THE SECOND-ORDER SPIN-ORBIT ENERGY CONTRIBUTION TO THE ZERO-FIELD-SPLITTING

A spin-triplet system can be quantized as $S_z = \{-1, 0, +1\}$, where the z quantization axis is chosen to be parallel with the symmetry axis of the NiV defect exhibiting D_{3d} point-group symmetry. The zero-field-splitting (ZFS) Hamiltonian can be described by the equation

$$\hat{D} = D\big(\hat{S}_z^2 - \tfrac{1}{3}S(S+1)\big), \tag{A1}$$

which yields $+\frac{1}{3}D$ and $-\frac{2}{3}D$ for $S_z = \pm 1$ and $S_z = 0$ eigenstates, respectively.

The value of D can be principally either negative or positive. Two effects may contribute to this interaction: the dipolar electron spin–electron spin interaction ($D_{\rm SS}$) and the (second-order) spin-orbit interaction ($D_{\rm LS}$). As we discussed in the main text, the order of magnitude of $D_{\rm SS}$ is GHz or μeV because the strength of dipolar interaction goes with the gyromagnetic factor of the electron and the interaction distance (localized spin density distribution). In NiV^0 defect, the D value is rather in the meV region, thus, we focus on the $D_{\rm LS}$ contribution.

We describe now the self-consistent calculus for $D_{\rm LS}$. We set the quantization axis to the [111] direction which coincides with the symmetry axis of the defect in diamond. In the usual spin-polarized DFT calculation one obtains the $S_z = \pm 1$ solution

$$E_{\rm tot}(|\uparrow\uparrow\rangle) = \langle\uparrow\uparrow|\hat{H}_{\rm el} + \hat{D}_{\rm LS}|\uparrow\uparrow\rangle = \tfrac{1}{3}D_{\rm LS} + C, \tag{A2}$$

where an arbitrary C constant is introduced which is the electronic total energy from $\hat{H}_{\rm el}$ Hamiltonian of system and $D_{\rm LS}$ is the spin-orbit correction as formulated in Eq. (A1).

Next, the two spins are individually rotated by 90° about the x axis. A spin-$\frac{1}{2}$ system will be $|\rightarrow\rangle = (|\uparrow\rangle + |\downarrow\rangle)/\sqrt{2}$ according to the rotation of a spinor-$\frac{1}{2}$ object. Thus, the $S_z = 1$ spin projection rotated to any axis perpendicular to [111] is

$$|\rightarrow\rightarrow\rangle = \frac{1}{2}\overbrace{|\uparrow\uparrow\rangle}^{S_z=+1} + \frac{1}{2}\overbrace{|\downarrow\downarrow\rangle}^{S_z=-1} + \frac{1}{\sqrt{2}}\Bigg(\overbrace{\frac{1}{\sqrt{2}}(|\uparrow\downarrow\rangle + |\downarrow\uparrow\rangle)}^{S_z=0}\Bigg). \tag{A3}$$

We assume that the C electronic energy does not depend on direction of the spin. Therefore, the total energy of the system will be

$$\begin{aligned} E_{\rm tot}(|\rightarrow\rightarrow\rangle) &= \langle\rightarrow\rightarrow|\hat{D}_{\rm LS} + \hat{H}_{\rm el}|\rightarrow\rightarrow\rangle \\ &= \frac{1}{4}\langle\uparrow\uparrow|\hat{D}_{\rm LS}|\uparrow\uparrow\rangle + \frac{1}{4}\langle\downarrow\downarrow|\hat{D}_{\rm LS}|\downarrow\downarrow\rangle \\ &\quad + \frac{1}{2}\left(\frac{1}{\sqrt{2}}(|\uparrow\downarrow\rangle + |\downarrow\uparrow\rangle)\right)\hat{D}_{\rm LS} \\ &\quad \times \left(\frac{1}{\sqrt{2}}(|\uparrow\downarrow\rangle + |\downarrow\uparrow\rangle)\right) + C \\ &= \frac{1}{12}D_{\rm LS} + \frac{1}{12}D_{\rm LS} - \frac{1}{6}D_{\rm LS} + C = C. \end{aligned} \tag{A4}$$

Thus, the value of $D_{\rm LS}$ can be directly calculated at *ab initio* level by

$$\begin{aligned} D_{\rm LS} &= 3(E_{\rm tot}(|\uparrow\uparrow\rangle) - E_{\rm tot}(|\rightarrow\rightarrow\rangle)) \\ &= 3(\langle\uparrow\uparrow|\hat{D}_{\rm LS}|\uparrow\uparrow\rangle - \langle\rightarrow\rightarrow|\hat{D}_{\rm LS}|\rightarrow\rightarrow\rangle), \end{aligned} \tag{A5}$$

where we combined Eqs. (A4) and (A2). In simple words, the rotated spin in Eq. (A4) is not an $S_z = 0$ eigenstate, thus, one needs to multiply the total-energy difference of the two self-consistent *ab initio* total energies by 3 in Eq. (A5).

We self-consistently calculated the total energy of the two spin configurations for NiV^0 defect. We obtained $D_{\rm LS}^{\rm HSE06} = 0.73$ meV and $D_{\rm LS}^{\rm PBE} = 1.35$ meV values by HSE06 and PBE functionals, respectively. Although, we claim that these values are inherently coming from the spin-orbit interaction but this is not obvious from the present derivation and methodology. In the next Appendix (Appendix B), we derive within perturbation theory how this interaction occurs between the triplet ground state and the singlet excited state, and how the energy gap between the two levels affects the final $D_{\rm LS}$ value.

APPENDIX B: SECOND-ORDER PERTURBATION THEORY FOR THE CONTRIBUTION OF SPIN-ORBIT INTERACTION IN THE ZERO-FIELD-SPLITTING FOR SPIN-1 SYSTEMS

We demonstrate the contribution of spin-orbit interaction in the zero-field splitting for spin-1 system on NiV^0 defect in diamond. The $S = 1$ state is associated with the $(e_u e_u)$ electronic configuration. The ground state is

$$|^3A_{2g}\rangle = \frac{1}{\sqrt{2}}\underbrace{(|e_{ux}e_{uy}\rangle - |e_{uy}e_{ux}\rangle)}_{|e_{u+}e_{u-}\rangle - |e_{u-}e_{u+}\rangle} \otimes \begin{cases} |\uparrow\uparrow\rangle \\ (|\uparrow\downarrow\rangle + |\downarrow\uparrow\rangle)/\sqrt{2}, \\ |\downarrow\downarrow\rangle \end{cases} \tag{B1}$$

where we introduced the $|e_{u\pm}\rangle = \frac{1}{\sqrt{2}}(|e_{ux}\rangle \pm i|e_{uy}\rangle)$ notation for the complex orbitals. The $|e_\pm\rangle$ orbitals depict the effective angular momentum of the system, that is, $\hat{L}_z|e_{u\pm}\rangle = \pm|e_{u\pm}\rangle$ [for visual interpretation see Fig. 1(b)]. The excited $|^1E_g\rangle$ singlet state can be expressed as

$$|^1E_g\rangle = \underbrace{\left\{\begin{matrix}(|e_xe_x\rangle - |e_ye_y\rangle)/\sqrt{2} \\ (|e_xe_y\rangle + |e_ye_x\rangle)/\sqrt{2}\end{matrix}\right\}}_{\{|e_-e_-\rangle;\,|e_+e_+\rangle\}} \otimes \frac{1}{\sqrt{2}}(|\uparrow\downarrow\rangle - |\downarrow\uparrow\rangle), \tag{B2}$$

whereas $|\,^1A_{1g}\rangle$ is

$$|^1A_{1g}\rangle = \frac{1}{\sqrt{2}}\underbrace{(|e_{ux}e_{uy}\rangle - |e_{uy}e_{ux}\rangle)}_{|e_{u+}e_{u-}\rangle + |e_{u-}e_{u+}\rangle} \otimes \frac{1}{\sqrt{2}}(|\uparrow\downarrow\rangle - |\downarrow\uparrow\rangle). \tag{B3}$$

The effective one-electron spin-orbit coupling operator is

$$\hat{h}_{\rm SOC} = \lambda_0\hat{L}_z\hat{S}_z, \tag{B4}$$

where $\hat{L}_z|e_{u\pm}\rangle$ acts on the orbital degrees of freedom and $\hat{S}_z$ acts on the electron spin. The Hamiltonian of the system is

then

$$\hat{H} = 0|^3A_{2g}\rangle\langle{}^3A_{2g}| + \Pi|^1E_g\rangle\langle{}^1E_g| + \Theta|^1A_{1g}\rangle\langle{}^1A_{1g}| + \hat{W}, \tag{B5}$$

where we introduced Π and Θ parameters for the energy position of the corresponding singlet states while leaving the triplet ground state's level as zero. Additionally, we define spin-orbit coupling into the $\hat{W}$ operator as $\hat{W} = \hat{h}^{(1)}_{\rm SOC} + \hat{h}^{(2)}_{\rm SOC}$ which includes $\hat{h}_{\rm SOC}$ single-particle operator from Eq. (B4) that acts on the first electron and second electron, respectively. Next, one has to treat the spin-orbit coupling as a perturbation and evaluate $\hat{W}$. The only nonzero spin-orbit matrix element occurs between $|^1A_{1g}\rangle$ singlet and the $S_z = 0$ substate of $|^3A_{2g}\rangle$ which goes as

$$\begin{aligned}&\langle{}^1A_{1g}|\hat{W}|^3A_{2g}(S_z=0)\rangle\\ &\quad= (\langle e_{u+}e_{u-}| + \langle e_{u-}e_{u+}|)(|\uparrow\downarrow\rangle - |\downarrow\uparrow\rangle)\\ &\qquad\times\lambda_0\big(\hat{L}^{(1)}_z\hat{S}^{(1)}_z + \hat{L}^{(2)}_z\hat{S}^{(2)}_z\big)\\ &\qquad\times(|e_{u+}e_{u-}\rangle - |e_{u-}e_{u+}\rangle)(|\uparrow\downarrow\rangle + |\downarrow\uparrow\rangle) = \lambda_0,\end{aligned} \tag{B6}$$

where $\hat{L}^{(1)}_z\hat{S}^{(1)}_z$ and $\hat{L}^{(2)}_z\hat{S}^{(2)}_z$ operators affect the first and second electrons' orbital and spin. Thus, according to second-order perturbation theory, $|^3A_{2g}(S_z=0)\rangle$ level is shifted downwards by λ_0/Θ energy (and $|^1A_{1g}\rangle$ level is shifted upwards with the same amount). Briefly, the spin-orbit part contribution to the ZFS is simplified to

$$D_{\rm LS} = \frac{\lambda_0^2}{\Theta}, \tag{B7}$$

where one can take the $\lambda_0 = 23.2$ meV intrinsic spin-orbit parameter of NiV^- as given in Sec. III C 1. We roughly approximate the position of $|^1A_{1g}\rangle$ singlet with the following *ab initio* calculations:

$$\Theta \approx E_{\rm tot}[\mathcal{A}|e^{\uparrow}_{ux}e^{\downarrow}_{ux}\rangle] - E_{\rm tot}[\mathcal{A}|e^{\uparrow}_{ux}e^{\uparrow}_{uy}\rangle] = 0.68\ \text{eV}, \tag{B8}$$

where $\mathcal{A}$ is the two-particle antisymmetrization operator, $\mathcal{A}|12\rangle = (|12\rangle - |21\rangle)/\sqrt{2}$, and $E_{\rm tot}[\dots]$ labels the DFT total energy of the corresponding single Slater-determinant state. We obtained $\Xi \approx 0.68$ eV by means of HSE06 functional. While the second term provides the triplet ground state that is a well-defined single Slater-determinant state, the first term is not an eigenstate of the system but an admixture of the two singlet states,

$$\begin{aligned}\mathcal{A}|e^{\uparrow}_{ux}e^{\downarrow}_{ux}\rangle &= \frac{1}{\sqrt{2}}|e_{ux}e_{ux}\rangle\otimes(|\uparrow\downarrow\rangle - |\downarrow\uparrow\rangle)\\ &= \frac{1}{\sqrt{2}}(|^1A_{1g}\rangle + |^1E_{gx}\rangle),\end{aligned} \tag{B9}$$

where $|^1E_{gx}\rangle = (|e_xe_x\rangle - |e_ye_y\rangle)/\sqrt{2}$ is one of the substates of the orbitally degenerate $|^1E_g\rangle$ multiplet as defined in Eq. (B2). Finally, the estimated ZFS from second-order perturbation theory yields $D^{\rm pert.}_{\rm LS} = 0.79$ meV by HSE06 functional. This value is about 0.06 meV higher than that obtained by self-consistent procedure (see Sec. III B 1). This can be expected as the first-order spin-orbit correction in the wave function

$$|\Psi\rangle^{(1)} = |^3A_{2g}(S_z=0)\rangle + \frac{\lambda_0}{\Theta}|^1A_{1g}\rangle \tag{B10}$$

is optimized self-consistently in our self-consistent procedure, which results in a lower total energy. The origin between the relatively large discrepancy in the calculated $D^{\rm PBE}_{\rm LS} = 1.35$ meV and $D^{\rm HSE06}_{\rm LS} = 0.73$ meV can be understood by the second-order perturbation theory approach. We find that $\Theta = 0.25$ eV at PBE DFT level, thus, the too-small energy gap between the triplet state and the corresponding singlet state will result in too large spin-orbit contribution to the ZFS. This underlines the need of such DFT functionals in these calculations which produce energy spacing between the ground state and excited states.

APPENDIX C: SPIN-ORBIT MIXING IN THE TRIPLET EXCITED STATE OF NiV^{2-} DEFECT

As described in Sec. III D the triplet ($|T\rangle$) and singlet ($|S\rangle$) excited states may mix with each other. The possible $|e_u\rangle$ hole and $|e_g\rangle$ electron two-particle wave functions with $\langle\hat{S}_z\rangle = 0$ projection are the following:

$$|T, m_S = 0\rangle = \frac{\mathcal{A}}{\sqrt{2}}\begin{cases}|e_{g+\uparrow}e_{u+\downarrow}\rangle + |e_{g+\downarrow}e_{u+\uparrow}\rangle,\\ |e_{g+\uparrow}e_{u-\downarrow}\rangle + |e_{g+\downarrow}e_{u-\uparrow}\rangle,\\ |e_{g-\uparrow}e_{u+\downarrow}\rangle + |e_{g-\downarrow}e_{u+\uparrow}\rangle,\\ |e_{g-\uparrow}e_{u-\downarrow}\rangle + |e_{g-\downarrow}e_{u-\uparrow}\rangle\end{cases} \tag{C1}$$

and

$$|S\rangle = \frac{\mathcal{A}}{\sqrt{2}}\begin{cases}|e_{g+\uparrow}e_{u+\downarrow}\rangle - |e_{g+\downarrow}e_{u+\uparrow}\rangle,\\ |e_{g+\uparrow}e_{u-\downarrow}\rangle - |e_{g+\downarrow}e_{u-\uparrow}\rangle,\\ |e_{g-\uparrow}e_{u+\downarrow}\rangle - |e_{g-\downarrow}e_{u+\uparrow}\rangle,\\ |e_{g-\uparrow}e_{u-\downarrow}\rangle - |e_{g-\downarrow}e_{u-\uparrow}\rangle,\end{cases} \tag{C2}$$

where $\mathcal{A}$ is the two-particle antisymmetrization operator: $\mathcal{A}|ab\rangle = (|ab\rangle - |ba\rangle)/\sqrt{2}$. The spin-orbit operator that connects the singlet and triplet levels is the following:

$$\hat{H}_{\rm SOC} = \lambda_u\hat{L}_{z(u)}\hat{S}_z + \lambda_g\hat{L}_{z(g)}\hat{S}_z, \tag{C3}$$

where the $\hat{L}_{z(u/g)}|e_\pm\rangle = \pm|e_{u/g\pm}\rangle$ angular momentum operators act individually for e_u and e_g orbitals, and $\hat{S}_z$ operators are the usual single-particle spin-$\frac{1}{2}$ operators: $\hat{S}_z|\uparrow\rangle = +\frac{1}{2}|\uparrow\rangle$, $\hat{S}_z|\downarrow\rangle = -\frac{1}{2}|\downarrow\rangle$. According to perturbation theory, the singlet states mix into the triplet states, i.e., $(\Psi^{(1)} = \frac{1}{\sqrt{1+c^2}}|T\rangle + c|S\rangle)$, by

$$\begin{aligned}\frac{\hat{H}_{\rm SOC}}{\Delta E}|T\rangle &= \frac{\hat{H}_{\rm SOC}}{\Delta E}\frac{\mathcal{A}|e_{g+\uparrow}e_{u+\downarrow}\rangle + \mathcal{A}|e_{g+\downarrow}e_{u+\uparrow}\rangle}{\sqrt{2}}\\ &= \frac{\lambda_g - \lambda_u}{2\Delta E}|S\rangle = c\times|S\rangle.\end{aligned} \tag{C4}$$

One may show the remaining off-diagonal matrix elements between the singlets and triplets,

$$\begin{aligned}&\langle T|\hat{H}_{\rm SOC}|S\rangle\\ &= \begin{pmatrix}\lambda_g - \lambda_u & 0 & 0 & 0\\ 0 & \lambda_g + \lambda_u & 0 & 0\\ 0 & 0 & -\lambda_g - \lambda_u & 0\\ 0 & 0 & 0 & -\lambda_g + \lambda_u\end{pmatrix},\end{aligned} \tag{C5}$$

thus, there are always two $S_z = 0$ triplet substates where λ_g and λ_u parameters mix the singlet additively $|\lambda_g| + |\lambda_u|$ regardless their sign that we used in Eq. (C3).

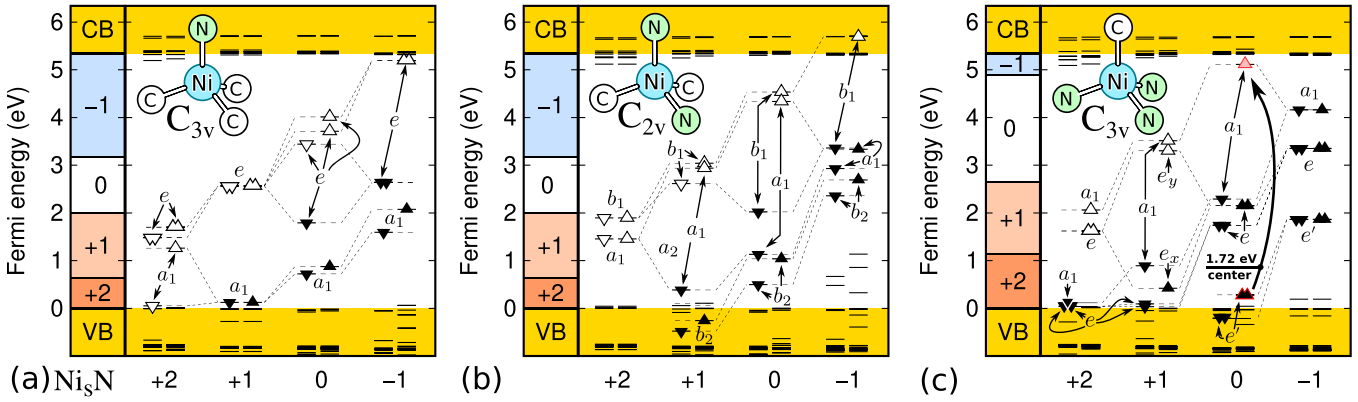

FIG. 7. Kohn-Sham levels of (a) Ni_sN_s, (b) $Ni_s(N_s)_2$, (c) $Ni_s(N_s)_3$ complexes. We denote the *ab initio* charge transition levels on the left bar for each figure. We also depict the excitation process for $Ni_s(N_s)_3^-$ that we associate with the NE4 EPR center and 1.72-eV optical center. We note that we lifted the C_{3v} symmetry constraint for $Ni_sN_s^0$ and $Ni_s(N_s)_3^+$, therefore, e_x (e_y) orbitals become a' (a'') in the lower C_{1h} symmetry.

Finally, we justify the c^2 prefactor in Eq. (8). The triplet excited state $|^3\widetilde{A}_{2u}\rangle$ now has singlet admixtures, thus, the spontaneous emission by means of time-dependent perturbation theory with $\hat{d}$ transition dipole operator acts only if the system stays in its singlet state

$$\begin{aligned}\tau^{-1} &\sim |\langle {}^1A_{1g}|\hat{d}|{}^3\widetilde{A}_{2u}\rangle|^2 \\ &= \left|\langle {}^1A_{1g}|\hat{d} \times \left(\frac{1}{\sqrt{1+c^2}}|T\rangle + c|S\rangle\right)\right|^2 \\ &= c^2 \times |\langle {}^1A_{1g}|\hat{d}|S\rangle|^2 = c^2 \times \frac{n\omega^3|\mu|^2}{3\pi\varepsilon_0}. \end{aligned} \quad \text{(C6)}$$

Thus, the optical transition probability to the $\langle {}^1A_{1g}|$ ground state has to be scaled by the c^2 factor.

APPENDIX D: ORIGIN OF THE NE4/AB1 EPR CENTER AND THE ASSOCIATED 1.72-EV OPTICAL CENTER

Here we discuss the possible models for the NE4 center. The NE4/AB1 EPR center has $S = \frac{1}{2}$ spin with C_{3v} symmetry and relatively isotropic g tensor with $g_\parallel = 2.0027(2)$ and $g_\perp = 2.0923(2)$ (Ref. [46]). This property significantly differs from that of NIRIM-2 EPR center with $g_\perp = 0$. We learned from our study that $g_\perp$ is quenched in NIRIM-2 EPR center because of the strong spin-orbit interaction in the orbital doublet ground state. This assumes that the ground state of NE4/AB1 EPR center should be an orbital singlet. On the other hand, the associated 1.72-eV optical center exhibits a doublet structure with an energy gap of 4.7 ± 0.1 meV (Ref. [50]). This indicates that the excited state should be then an orbital doublet. Besides the NE4/AB1 EPR center was observed in HPHT diamonds where the concentration of nitrogen is high. Thus, it cannot be excluded that NE4/AB1 EPR center may contain nitrogen.

We conclude that the ground state should be an $^2A_1$ (or $^2A_2$) within C_{3v} symmetry for NE4/AB1 EPR center. Simple nickel substitutional defect or nickel split-vacancy defects do not form such ground state as discussed in the main text. The NiV defects with three nitrogens substituting nearby carbon atoms were already identified in the EPR spectrum. The next feasible models within the given constraints are either substitutional nickel with a substitutional nitrogen atom (Ni_sN_s) or three substitutional nitrogen atoms [$Ni_s(N_s)_3$]. We found that none of the charge states of Ni_sN_s produce $^2A_1$ ground state. However, the $Ni_s(N_s)_3^0$ defect exhibits $^2A_1$ ground state, and the neutral charge state is stable in N-doped diamond [see Fig. 7(c)]. Thus, our tentative model for the NE4 EPR center is the $Ni_s(N_s)_3^0$ defect that we discuss further.

The g tensor of $Ni_s(N_s)_3^0$ was determined with a method as described in our previous study [101]. In particular, the g tensor is modified from the free-electron value $g_S = 2.002319$ because of the orbital moment of the Ni $3d$ orbitals in which the defect wave function is largely localized. This justifies

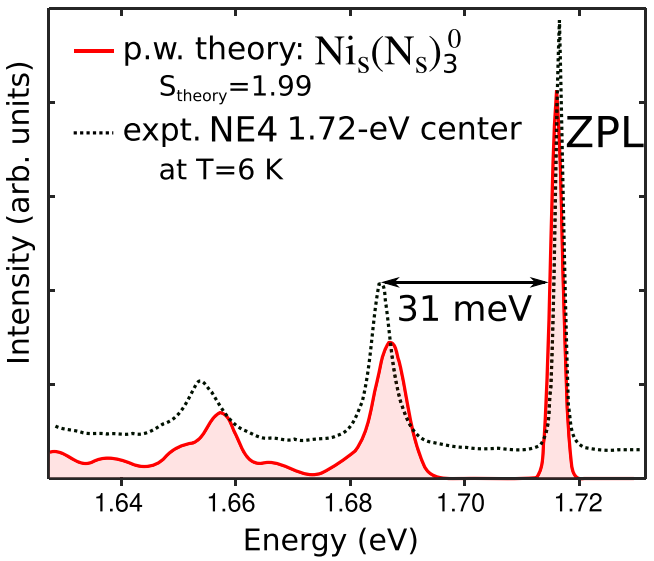

FIG. 8. *Ab initio* PL spectrum of $Ni_s(N_s)_3^0$ defect within Huang-Rhys theory with taking into account only the symmetric (A_{1g}) phonons. ZPL stands for the zero-phonon line where the theoretical ZPL was aligned to the experimental one at 1.717 eV for the sake of clarity in the comparison of the corresponding phonon sidebands. We applied 1-meV Gaussian broadening and its area under curve was fitted to the experimental data. Additionally, we applied 3.5-meV broadening for the theoretical sideband. Experimental data are taken from Fig. 11 in Ref. [50].

to calculate the total orbital moment ($\langle \hat{L}_{x,y,z} \rangle$) of the defect within the PAW sphere of the ions where the largest contribution comes from the Ni ion. Because of C_{3v} symmetry $\langle \hat{L}_x \rangle = \langle \hat{L}_y \rangle = \langle \hat{L}_\perp \rangle$. The main components of the g tensor can be given as $g_\parallel = g_S + 2\langle \hat{L}_z \rangle$ and $g_\perp = g_S + 2\langle \hat{L}_\perp \rangle$. We finally obtain $g_\parallel = 2.0058$ and $g_\perp = 2.0942$ which are in good agreement with the experimental data.

Additionally, we determined the hyperfine coupling parameters for the three equivalent ^{14}N isotopes: $A_{xx} = -2.0$ MHz $\parallel$ [1 −1 0], $A_{yy} = -1.6$ MHz $\parallel$ [0.13 0.13 −0.98], $A_{zz} = 2.9$ MHz $\parallel$ [0.70 0.70 −0.18], where we depict hyperfine main axes by the directions expressed in diamond crystal axes inside the brackets. The 99.6% natural abundance of ^{14}N isotopes ensures that the hyperfine splittings due to ^{14}N should be observable. However, as we mentioned in the Introduction, no hyperfine splittings were observed for the NE4/AB1 center. However, the Lorentzians of NE4/AB1 center exhibit linewidths approximately ∼10 MHz (∼0.4 mT) in Refs. [52,102]. Our results imply that the ^{14}N hyperfine satellite may result in such as broadening. Most of the spin density lies on the Ni atom and its first-neighbor carbon atoms. Thus, we report $A_\parallel = 60.1$ MHz, $A_\perp = 8.5$ MHz for ^{13}C and $A_\parallel = -94$ MHz, $A_\perp = 146$ MHz for ^{61}Ni nuclear spins. Here, we suggest additional EPR measurements for the NE4/AB1 center to unambiguously prove the $\mathrm{Ni_s(N_s)_3^0}$ model.

Furthermore, the $\mathrm{Ni_s(N_s)_3^0}$ defect system can be optically excited [see Fig. 7(c)]. According to our ΔSCF results, the $\mathrm{Ni_s(N_s)_3^0}$ has two excited states. There is an ^2E orbital doublet approximately above the ^2A ground state by ∼0.45 eV and there is an additional one at $^2E'$ at ∼1.7 eV. We note that we had convergence issues (∼0.15 eV deviation) in these excitation energies because the e and e' Kohn-Sham orbitals belong to the same representation in C_{3v} symmetry. That is, we see internal rotations between e and e' orbitals during the electronic self-consistent cycles that we primarily see as the source numerical instability. To overcome this limitation we applied a time-dependent DFT (TDDFT) calculation on a $\mathrm{NiN_3C_{449}H_{228}^0}$ nanodiamond model by means of the PBE0 hybrid functional [103] as implemented in the TURBOMOLE code as we described in Ref. [53]. According to our TTDFT results, the first ^2E level is at 0.63 eV and the second is at $^2E'$ 1.77 eV without geometry relaxation which agrees well with our ΔSCF result in the supercell model.

We were able to determine the spin-orbit parameters for the system within the PBE kernel in the 512-atom supercell that was sufficiently large for convergent spin-orbit parameters to for NiV^- (see Fig. 2). We placed a hole on the e or e' single-particle levels during a ΔSCF calculation to determine the spin-orbit splitting. According to our results, the e orbital exhibits $\lambda_e = 21.9$ meV spin-orbit splitting while e' exhibits $\lambda'_e = 14.6$ meV. However, these intrinsic values need to be reduced by the Ham effect [104,105] similarly that we did for NiV^- in Sec. III C 2. Unfortunately, even TDDFT procedure suffered from numerical instability with C_{3v} constraint enforced on the atomic positions, thus, we were not able to determine the Jahn-Teller nature of the system and thus the Ham reduction p factor. One may only compare the experimental $\lambda_{\mathrm{expt}} = 4.7$ meV [50] data with the calculated $\lambda'_e = 14.6$ meV intrinsic spin-orbit coupling which assumes $0 < p \approx 0.32 < 1$ Ham reduction factor.

Furthermore, we determined the vibronic sideband of the $^2A \leftrightarrow {}^2E'$ optical transition by means of Huang-Rhys theory (see Fig. 8). We constrained C_{3v} symmetry on the excited-state geometry relaxation and smeared the e hole by 50%-50% on the e_x and e_y orbitals depicted in Fig. 7(c). We note that because the HSE06 did not converge for the system, we used only PBE functional to determine the relaxation. One can clearly observe the nickel-related 31-meV localized effective vibration mode in the PL spectrum.

In summary, although we cannot claim an unambiguous identification for the NE4 EPR center and 1.72-eV optical center, we provide numerous features in the calculated magneto-optical spectra that show the fingerprints of the centers. Namely, (i) we were able to identify the origin of splitting in the PL spectrum (spin-orbit coupling); (ii) we identify a 30-meV localized nickel vibration mode in the simulated phonon sideband; (iii) the simulated $g_\perp$, $g_\parallel$ reproduces the experimental data. Understanding the characteristic hyperfine satellites from ^{14}N nuclear spins should be further studied in the experiments. In our interpretation, the hyperfine satellites of ^{14}N nuclear spins cause the broadening of the main EPR line in NE4/AB1 EPR centers. On the other hand, ^{13}C and ^{61}Ni satellites exhibit much larger hyperfine splittings but their natural abundance is only ∼1%, thus is barely visible in the EPR spectrum. Therefore, we suggest to revisit the fine hyperfine satellites of NE4/AB1 EPR center for unambiguous identification.

[1] A. Yelisseyev and H. Kanda, Optical centers related to 3d transition metals in diamond, New Diamond Front. Carbon Technol. **17**, 127 (2007).

[2] A. M. Zaitsev, *Optical Properties of Diamond: A Data Handbook* (Springer, New York, 2013).

[3] V. Nadolinny, A. Komarovskikh, and Y. Palyanov, Incorporation of large impurity atoms into the diamond crystal lattice: EPR of split-vacancy defects in diamond, Crystals **7**, 237 (2017).

[4] G. Thiering and A. Gali, *Ab Initio* Magneto-Optical Spectrum of Group-iv Vacancy Color Centers in Diamond, Phys. Rev. X **8**, 021063 (2018).

[5] Á. Gali, *Ab initio* theory of the nitrogen-vacancy center in diamond, Nanophotonics **8**, 1907 (2019).

[6] G. Thiering and A. Gali, Color centers in diamond for quantum applications, in *Diamond for Quantum Applications Part 1* (Elsevier, Amsterdam, 2020), pp. 1–36.

[7] E. Londero, E. Bourgeois, M. Nesladek, and A. Gali, Identification of nickel-vacancy defects by combining experimental and *ab initio* simulated photocurrent spectra, Phys. Rev. B **97**, 241202(R) (2018).

[8] E. Bourgeois, A. Jarmola, P. Siyushev, M. Gulka, J. Hruby, F. Jelezko, D. Budker, and M. Nesladek, Photoelectric

detection of electron spin resonance of nitrogen-vacancy centres in diamond, Nat. Commun. **6**, 8577 (2015).

[9] M. Gulka, E. Bourgeois, J. Hruby, P. Siyushev, G. Wachter, F. Aumayr, P. R. Hemmer, A. Gali, F. Jelezko, M. Trupke, and M. Nesladek, Pulsed Photoelectric Coherent Manipulation and Detection of N$-v$ Center Spins in Diamond, Phys. Rev. Appl. **7**, 044032 (2017).

[10] E. Bourgeois, M. Gulka, and M. Nesladek, Photoelectric detection and quantum readout of nitrogen-vacancy center spin states in diamond, Adv. Opt. Mater. **8**, 1902132 (2020).

[11] P. Siyushev, M. Nesladek, E. Bourgeois, M. Gulka, J. Hruby, T. Yamamoto, M. Trupke, T. Teraji, J. Isoya, and F. Jelezko, Photoelectrical imaging and coherent spin-state readout of single nitrogen-vacancy centers in diamond, Science **363**, 728 (2019).

[12] H. Morishita, S. Kobayashi, M. Fujiwara, H. Kato, T. Makino, S. Yamasaki, and N. Mizuochi, Room temperature electrically detected nuclear spin coherence of NV centres in diamond, Sci. Rep. **10**, 792 (2020).

[13] M. Gulka, D. Wirtitsch, V. Ivády, J. Vodnik, J. Hruby, G. Magchiels, E. Bourgeois, A. Gali, M. Trupke, and M. Nesladek, Room-temperature control and electrical readout of individual nitrogen-vacancy nuclear spins, Nat. Commun. **12**, 4421 (2021).

[14] J. H. N. Loubser and W. P. van Ryneveld, Electron spin resonance of nickel in synthetic diamonds, Nature (London) **211**, 517 (1966).

[15] M. I. Samoilovich, G. N. Bezrukov, and V. P. Butuzov, Electron paramagnetic resonance of nickel in synthetic diamond, Zh. Eksp. Teor. Fiz. **14**, 551 (1971) [JETP Lett. **14**, 379 (1971)].

[16] J. E. Lowther, Nickel defect centers in diamond, Phys. Rev. B **51**, 91 (1995).

[17] R. Larico, J. Justo, W. Machado, and L. Assali, An *ab initio* investigation on nickel impurities in diamond, Phys. B (Amsterdam) **340-342**, 84 (2003).

[18] R. Larico, L. V. C. Assali, W. V. M. Machado, and J. F. Justo, Isolated nickel impurities in diamond: A microscopic model for the electrically active centers, Appl. Phys. Lett. **84**, 720 (2004).

[19] R. Larico, L. Assali, W. Machado, and J. Justo, Nickel impurities in diamond: a FP-LAPW investigation, Comput. Mater. Sci. **30**, 62 (2004).

[20] R. Larico, L. V. C. Assali, W. V. M. Machado, and J. F. Justo, Erratum: isolated nickel impurities in diamond: A microscopic model for the electrically active centers, Appl. Phys. Lett. **85**, 6293 (2004).

[21] T. Chanier and A. Gali, *Ab initio* characterization of a Ni-related defect in diamond: The W8 center, Phys. Rev. B **87**, 245206 (2013).

[22] A. T. Collins, H. Kanda, J. Isoya, C. Ammerlaan, and J. van Wyk, Correlation between optical absorption and EPR in high-pressure diamond grown from a nickel solvent catalyst, Diam. Relat. Mater. **7**, 333 (1998).

[23] M. H. Nazaré, J. C. Lopes, and H. Kanda, Nickel related absorption lines in high-pressure synthetic diamond, MRS Proc. **339**, 625 (1994).

[24] M. Nazaré, J. Lopes, and A. Neves, Nickel related defects in diamond: The 2.51 eV band, Physica B (Amsterdam) **308-310**, 616 (2001).

[25] E. Pereira, L. Santos, L. Pereira, D. Hofmann, P. Christmann, W. Stadler, and B. Meyer, Slow emission of the 2.56 eV centre in synthetic diamond, Diam. Relat. Mater. **4**, 53 (1994).

[26] M. H. Nazare, P. W. Mason, G. D. Watkins, and H. Kanda, Optical detection of magnetic resonance of nitrogen and nickel in high-pressure synthetic diamond, Phys. Rev. B **51**, 16741 (1995).

[27] R. Larico, J. F. Justo, W. V. M. Machado, and L. V. C. Assali, Electronic properties and hyperfine fields of nickel-related complexes in diamond, Phys. Rev. B **79**, 115202 (2009).

[28] J. P. Goss, P. R. Briddon, R. Jones, and S. Öberg, The lattice location of ni in diamond: A theoretical study, J. Phys.: Condens. Matter **16**, 4567 (2004).

[29] A. T. Collins and P. M. Spear, The 1.40 eV and 2.56 eV centres in synthetic diamond, J. Phys. C: Solid State Phys. **16**, 963 (1983).

[30] P. Plochocka, O. Portugall, P. Y. Solane, E. Gheeraert, L. Ranno, E. Bustarret, N. Bruyant, I. Breslavetz, D. K. Maude, H. Kanda, and G. L. J. A. Rikken, High-field magnetospectroscopy to probe the 1.4-eV Ni color center in diamond, Phys. Rev. B **86**, 045203 (2012).

[31] P. J. Dean, Bound excitons and donor-acceptor pairs in natural and synthetic diamond, Phys. Rev. **139**, A588 (1965).

[32] I. Kupriyanov, V. Gusev, Y. Borzdov, A. Kalinin, and Y. Pal'yanov, Photoluminescence study of annealed nickel- and nitrogen-containing synthetic diamond, Diam. Relat. Mater. **8**, 1301 (1999).

[33] J. Isoya, H. Kanda, and Y. Uchida, EPR studies of interstitial ni centers in synthetic diamond crystals, Phys. Rev. B **42**, 9843 (1990).

[34] L. Paslovsky and J. E. Lowther, Optical dichroism of nickel in diamond, J. Phys.: Condens. Matter **4**, 775 (1992).

[35] K. Iakoubovskii and G. Davies, Vibronic effects in the 1.4$-$eV optical center in diamond, Phys. Rev. B **70**, 245206 (2004).

[36] T. Pawlik, C. Noble, and J.-M. Spaeth, Optically detected electron paramagnetic resonance of Ni-related defects in synthetic diamond crystals, J. Phys.: Condens. Matter **10**, 9833 (1998).

[37] E. Pereira and L. Santos, The 2.96 eV centre in diamond, Physica B (Amsterdam) **185**, 222 (1993).

[38] H. Kanda and K. Watanabe, Distribution of nickel related luminescence centers in HPHT diamond, Diam. Relat. Mater. **8**, 1463 (1999).

[39] D. M. Hofmann, W. Stadler, B. K. Meyer, L. Pereira, L. Santos, and E. Pereira, A spin resonance study of the 2.9 eV luminescence centers in natural and synthetic diamond, MRS Proc **339**, 619 (1994).

[40] V. Nadolinny, J. Baker, M. Newton, and H. Kanda, EPR studies of a nickel–boron centre in synthetic diamond, Diam. Relat. Mater. **11**, 627 (2002).

[41] K. Iakoubovskii, Ni-vacancy defect in diamond detected by electron spin resonance, Phys. Rev. B **70**, 205211 (2004).

[42] M. I. Rakhmanova, V. A. Nadolinny, and O. P. Yuryeva, Impurity centers in synthetic and natural diamonds with a system of electron-vibronic lines at 418 nm in luminescence spectra, Phys. Solid State **55**, 127 (2013).

[43] J. Isoya, H. Kanda, and Y. Morita, esr studies of point defects in synthetic diamond crystals, in *Advances in New Diamond Science and Technology (Proceedings of the Fourth International Conference on New Diamond Science and Technology)*, edited by S. Saito *et al.* (MYU, Tokyo, 1994), pp. 351–354.

[44] S. C. Lawson, H. Kanda, and M. Sekita, New nickel-related optical absorption in high-pressure synthetic diamond, Philos. Mag. B **68**, 39 (1993).

[45] V. Nadolinny and A. Yelisseyev, Structure and creation conditions of complex nitrogen-nickel defects in synthetic diamonds, Diam. Relat. Mater. **3**, 1196 (1994).

[46] W. Gehlhoff and R. N. Pereira, The identity of the AB1 and NE4 electron paramagnetic resonance spectra in high-pressure high-temperature diamond, J. Phys.: Condens. Matter **14**, 13751 (2002).

[47] A. Neves, R. Pereira, N. Sobolev, M. Nazaré, W. Gehlhoff, A. Näser, and H. Kanda, New paramagnetic defects in synthetic diamonds grown using nickel catalyst, Physica B (Amsterdam) **273-274**, 651 (1999).

[48] A. Neves, R. Pereira, N. Sobolev, M. Nazaré, W. Gehlhoff, A. Näser, and H. Kanda, New paramagnetic centers in annealed high-pressure synthetic diamond, Diam. Relat. Mater. **9**, 1057 (2000).

[49] R. Pereira, A. Neves, W. Gehlhoff, N. Sobolev, L. Rino, and H. Kanda, Annealing study of the formation of nickel-related paramagnetic defects in diamond, Diam. Relat. Mater. **11**, 623 (2002).

[50] A. Yelisseyev, S. Lawson, I. Sildos, A. Osvet, V. Nadolinny, B. Feigelson, J. Baker, M. Newton, and O. Yuryeva, Effect of HPHT Annealing on the Photoluminescence of Synthetic Diamonds Grown in the Fe–ni–c System, Diam. Relat. Mater. **12**, 2147 (2003).

[51] V. A. Nadolinny, A. P. Yelisseyev, J. M. Baker, M. E. Newton, D. J. Twitchen, S. C. Lawson, O. P. Yuryeva, and B. N. Feigelson, A study of 13c hyperfine structure in the EPR of nickel-nitrogen-containing centres in diamond and correlation with their optical properties, J. Phys.: Condens. Matter **11**, 7357 (1999).

[52] V. A. Nadolinny, A. P. Yelisseyev, O. P. Yuryeva, and B. N. Feygelson, EPR study of the transformations in nickel containing centres at heated synthetic diamonds, Appl. Magn. Reson. **12**, 543 (1997).

[53] G. Thiering, E. Londero, and A. Gali, Single nickel-related defects in molecular-sized nanodiamonds for multicolor bioimaging: An *ab initio* study, Nanoscale **6**, 12018 (2014).

[54] V. A. Nadolinny, J. M. Baker, O. P. Yuryeva, M. E. Newton, D. J. Twitchen, and Y. N. Palyanov, EPR study of the peculiarities of incorporating transition metal ions into the diamond structure, Appl. Magn. Reson. **28**, 365 (2005).

[55] K. Iakoubovskii, A. Stesmans, B. Nouwen, and G. J. Adriaenssens, ESR and optical evidence for a Ni vacancy center in CVD diamond, Phys. Rev. B **62**, 16587 (2000).

[56] G. Kresse and J. Furthmüller, Efficient iterative schemes for *ab initio* total-energy calculations using a plane-wave basis set, Phys. Rev. B **54**, 11169 (1996).

[57] P. E. Blöchl, Projector augmented-wave method, Phys. Rev. B **50**, 17953 (1994).

[58] O. Bengone, M. Alouani, P. Blöchl, and J. Hugel, Implementation of the projector augmented-wave LDA+U method: Application to the electronic structure of NiO, Phys. Rev. B **62**, 16392 (2000).

[59] A. Gali, Identification of individual ^{13}c isotopes of nitrogen-vacancy center in diamond by combining the polarization studies of nuclear spins and first-principles calculations, Phys. Rev. B **80**, 241204(R) (2009).

[60] J. Heyd, G. E. Scuseria, and M. Ernzerhof, Hybrid functionals based on a screened coulomb potential, J. Chem. Phys. **118**, 8207 (2003).

[61] A. V. Krukau, O. A. Vydrov, A. F. Izmaylov, and G. E. Scuseria, Influence of the exchange screening parameter on the performance of screened hybrid functionals, J. Chem. Phys. **125**, 224106 (2006).

[62] P. Deák, B. Aradi, T. Frauenheim, E. Janzén, and A. Gali, Accurate defect levels obtained from the HSE06 range-separated hybrid functional, Phys. Rev. B **81**, 153203 (2010).

[63] A. Gali, E. Janzén, P. Deák, G. Kresse, and E. Kaxiras, Theory of Spin-Conserving Excitation of the $N-V^-$ center in Diamond, Phys. Rev. Lett. **103**, 186404 (2009).

[64] G. Thiering and A. Gali, Complexes of silicon, vacancy, and hydrogen in diamond: A density functional study, Phys. Rev. B **92**, 165203 (2015).

[65] G. Makov and M. C. Payne, Periodic boundary conditions in *ab initio* calculations, Phys. Rev. B **51**, 4014 (1995).

[66] S. Lany and A. Zunger, Assessment of correction methods for the band-gap problem and for finite-size effects in supercell defect calculations: Case studies for ZnO and GaAs, Phys. Rev. B **78**, 235104 (2008).

[67] K. Huang and A. Rhys, Theory of light absorption and non-radiative transitions in f-centres, Proc. R. Soc. A **204**, 406 (1950).

[68] A. Alkauskas, B. B. Buckley, D. D. Awschalom, and C. G. V. de Walle, First-principles theory of the luminescence lineshape for the triplet transition in diamond nv centres, New J. Phys. **16**, 073026 (2014).

[69] J. P. Perdew, K. Burke, and M. Ernzerhof, Generalized Gradient Approximation made Simple, Phys. Rev. Lett. **77**, 3865 (1996).

[70] G. Thiering and A. Gali, *Ab initio* calculation of spin-orbit coupling for an NV center in diamond exhibiting dynamic Jahn-Teller effect, Phys. Rev. B **96**, 081115(R) (2017).

[71] Q. C. Qiu and A. Ceulemans, The {e ⊗ e}⊗ e vibronic coupling case: A prototypal product jahn-teller system, in *Vibronic Interactions: Jahn-Teller Effect in Crystals and Molecules* (Springer, Netherlands, 2001), pp. 97–102.

[72] G. Thiering and A. Gali, The (eg ⊗ eu) ⊗ eg product jahn–teller effect in the neutral group-IV vacancy quantum bits in diamond, npj Comput. Mater. **5**, 18 (2019).

[73] I. Harris, C. J. Ciccarino, J. Flick, D. R. Englund, and P. Narang, Group-iii quantum defects in diamond are stable spin-1 color centers, Phys. Rev. B **102**, 195206 (2020).

[74] K. Szász, T. Hornos, M. Marsman, and A. Gali, Hyperfine coupling of point defects in semiconductors by hybrid density functional calculations: The role of core spin polarization, Phys. Rev. B **88**, 075202 (2013).

[75] M. L. Munzarová, P. Kubáček, and M. Kaupp, Mechanisms of EPR hyperfine coupling in transition metal complexes, J. Am. Chem. Soc. **122**, 11900 (2000).

[76] O. V. Yazyev, I. Tavernelli, L. Helm, and U. Röthlisberger, Core spin-polarization correction in pseudopotential-based electronic structure calculations, Phys. Rev. B **71**, 115110 (2005).

[77] J. P. Goss, R. Jones, S. J. Breuer, P. R. Briddon, and S. Öberg, The Twelve-Line 1.682 Ev Luminescence Center in Diamond and the Vacancy-Silicon Complex, Phys. Rev. Lett. **77**, 3041 (1996).

[78] B. C. Rose, G. Thiering, A. M. Tyryshkin, A. M. Edmonds, M. L. Markham, A. Gali, S. A. Lyon, and N. P. de Leon, Strongly anisotropic spin relaxation in the neutral silicon vacancy center in diamond, Phys. Rev. B **98**, 235140 (2018).

[79] Z.-H. Zhang, P. Stevenson, G. m. H. Thiering, B. C. Rose, D. Huang, A. M. Edmonds, M. L. Markham, S. A. Lyon, A. Gali, and N. P. de Leon, Optically Detected Magnetic Resonance in Neutral Silicon Vacancy Centers in Diamond Via Bound Exciton States, Phys. Rev. Lett. **125**, 237402 (2020).

[80] G. m. H. Thiering and A. Gali, Theory of the optical spin-polarization loop of the nitrogen-vacancy center in diamond, Phys. Rev. B **98**, 085207 (2018).

[81] K. W. H. Stevens, On the magnetic properties of covalent xy 6 complexes, Proc. R. Soc. London A **219**, 542 (1953).

[82] V. Weisskopf and E. Wigner, Berechnung der naturlichen linienbreite auf grund der diracschen lichttheorie, Z. Phys. **63**, 54 (1930).

[83] M. D. Crossfield, Ph.D. thesis, University of London, 1981.

[84] C. J. Ciccarino, J. Flick, I. B. Harris, M. E. Trusheim, D. R. Englund, and P. Narang, Strong spin-orbit quenching via the product Jahn-Teller effect in neutral group IV qubits in diamond, npj Quantum Mater. **5**, 75 (2020).

[85] H. J. Monkhorst and J. D. Pack, Special points for brillouin-zone integrations, Phys. Rev. B **13**, 5188 (1976).

[86] S. Häußler, G. Thiering, A. Dietrich, N. Waasem, T. Teraji, J. Isoya, T. Iwasaki, M. Hatano, F. Jelezko, A. Gali, and A. Kubanek, Photoluminescence excitation spectroscopy of SiV- and GeV- color center in diamond, New J. Phys. **19**, 063036 (2017).

[87] J. Görlitz, D. Herrmann, G. Thiering, P. Fuchs, M. Gandil, T. Iwasaki, T. Taniguchi, M. Kieschnick, J. Meijer, M. Hatano, A. Gali, and C. Becher, Spectroscopic investigations of negatively charged tin-vacancy centres in diamond, New J. Phys. **22**, 013048 (2020).

[88] M. H. Nazaré, A. J. Neves, and G. Davies, Optical studies of the 1.40-ev ni center in diamond, Phys. Rev. B **43**, 14196 (1991).

[89] G. F. Koster, J. O. Dimmock, R. G. Wheeler, and H. Statz, *Properties of the Thirty-two Point Groups*, Vol. 24 (MIT Press, Cambridge, MA, 1963).

[90] P. W. Atkins, M. S. Child, and C. S. G. Phillips, *Tables for Group Theory*, Vol. 6 (Oxford University Press, Oxford, 1970).

[91] J. N. Becker, J. Görlitz, C. Arend, M. Markham, and C. Becher, Ultrafast all-optical coherent control of single silicon vacancy colour centres in diamond, Nat. Commun. **7**, 13512 (2016).

[92] J. N. Becker and C. Becher, Coherence properties and quantum control of silicon vacancy color centers in diamond, Phys. Status Solidi A **214**, 1700586 (2017).

[93] J. N. Becker, B. Pingault, D. Groß, M. Gündoğan, N. Kukharchyk, M. Markham, A. Edmonds, M. Atatüre, P. Bushev, and C. Becher, All-Optical Control of the Silicon-Vacancy Spin in Diamond at Millikelvin Temperatures, Phys. Rev. Lett. **120**, 053603 (2018).

[94] K. D. Jahnke, A. Sipahigil, J. M. Binder, M. W. Doherty, M. Metsch, L. J. Rogers, N. B. Manson, M. D. Lukin, and F. Jelezko, Electron–phonon processes of the silicon-vacancy centre in diamond, New J. Phys. **17**, 043011 (2015).

[95] C. Hepp, T. Müller, V. Waselowski, J. N. Becker, B. Pingault, H. Sternschulte, D. Steinmüller-Nethl, A. Gali, J. R. Maze, M. Atatüre, and C. Becher, Electronic Structure of the Silicon Vacancy Color Center in Diamond, Phys. Rev. Lett. **112**, 036405 (2014).

[96] Y. Zhou, A. Rasmita, K. Li, Q. Xiong, I. Aharonovich, and W. bo Gao, Coherent control of a strongly driven silicon vacancy optical transition in diamond, Nat. Commun. **8**, 14451 (2017).

[97] T. Iwasaki, Y. Miyamoto, T. Taniguchi, P. Siyushev, M. H. Metsch, F. Jelezko, and M. Hatano, Tin-Vacancy Quantum Emitters in Diamond, Phys. Rev. Lett. **119**, 253601 (2017).

[98] M. E. Trusheim, B. Pingault, N. H. Wan, M. Gündoğan, L. De Santis, R. Debroux, D. Gangloff, C. Purser, K. C. Chen, M. Walsh, J. J. Rose, J. N. Becker, B. Lienhard, E. Bersin, I. Paradeisanos, G. Wang, D. Lyzwa, A. R.-P. Montblanch, G. Malladi, H. Bakhru *et al.*, Transform-Limited Photons from a Coherent Tin-Vacancy Spin in Diamond, Phys. Rev. Lett. **124**, 023602 (2020).

[99] D. D. Sukachev, A. Sipahigil, C. T. Nguyen, M. K. Bhaskar, R. E. Evans, F. Jelezko, and M. D. Lukin, Silicon-Vacancy Spin Qubit in Diamond: A Quantum Memory Exceeding 10 ms with Single-Shot State Readout, Phys. Rev. Lett. **119**, 223602 (2017).

[100] M. H. Metsch, K. Senkalla, B. Tratzmiller, J. Scheuer, M. Kern, J. Achard, A. Tallaire, M. B. Plenio, P. Siyushev, and F. Jelezko, Initialization and Readout of Nuclear Spins Via a Negatively Charged Silicon-Vacancy Center in Diamond, Phys. Rev. Lett. **122**, 190503 (2019).

[101] A. Csóré and A. Gali, *Ab initio* determination of pseudospin for paramagnetic defects in sic, Phys. Rev. B **102**, 241201(R) (2020).

[102] K. Iakoubovskii and A. T. Collins, Alignment of ni- and co-related centres during the growth of high-pressure–high-temperature diamond, J. Phys.: Condens. Matter **16**, 6897 (2004).

[103] J. P. Perdew, M. Ernzerhof, and K. Burke, Rationale for mixing exact exchange with density functional approximations, J. Chem. Phys. **105**, 9982 (1996).

[104] F. S. Ham, Dynamical jahn-teller effect in paramagnetic resonance spectra: Orbital reduction factors and partial quenching of spin-orbit interaction, Phys. Rev. **138**, A1727 (1965).

[105] F. S. Ham, Effect of linear Jahn-Teller coupling on paramagnetic resonance in a ^2e state, Phys. Rev. **166**, 307 (1968).